


Original Research

Identification of *TRIM59* as a Key Biomarker for Ferroptosis Resistance and Immunotherapy Response in Bladder Cancer via Multi-Omics Integration and Machine Learning

Jianyuan Lei¹, Ping Wang¹, Yanchun Qu², Xingfen Wang², Xianglian Zhang², Hui Li^{3,*}, Pengyu Zhang^{3,*} 

¹Department of Pathology, Shaanxi Provincial People's Hospital, 710068 Xi'an, Shaanxi, China

²Department of Pathology, The Second Hospital of Tianjin Medical University, 300211 Tianjin, China

³Department of Blood Transfusion, Tianjin Medical University Cancer Institute & Hospital, National Clinical Research Center for Cancer, Tianjin's Clinical Research Center for Cancer, Key Laboratory of Cancer Prevention and Therapy, Tianjin, 300060 Tianjin, China

*Correspondence: zpysxk@yeah.net (Hui Li); zhangpengyu@tjmuch.com (Pengyu Zhang)

Academic Editor: Alfonso Urbanucci

Submitted: 30 June 2025 Revised: 12 September 2025 Accepted: 19 September 2025 Published: 29 September 2025

Abstract

Background: Bladder cancer (BCa) is a highly heterogeneous malignancy, and precision treatment remains challenging. Identifying molecular biomarkers and risk factors is essential for improving prognosis and therapeutic strategies. **Methods:** We integrated expression quantitative trait loci (eQTL) data with Mendelian randomization (MR) analysis to identify candidate risk genes associated with BCa. Subsequently, a prognostic risk model was developed using machine learning methods to explore its correlation with molecular features, immune cell infiltration, and ferroptosis-related pathways. Based on these findings, the Tripartite Motif Containing 59 (*TRIM59*) protein was selected for further experimental validation. The functional role of *TRIM59* in BCa progression was further investigated using MTT assays in BCa cell lines. Additionally, western blotting (WB) was conducted to confirm the potential association between *TRIM59* expression and ferroptosis regulation. **Results:** The risk model identified distinct signaling pathways that differentiate the high-risk and low-risk BCa groups. The low-risk group demonstrated greater infiltration of CD8+ T cells. Conversely, the high-risk group exhibited enhanced immune evasion, as evidenced by increased infiltration of macrophages and fibroblasts. Furthermore, *TRIM59* exerts a regulatory influence on ferroptosis progression in BCa by modulating key genes involved in this process, including Solute Carrier Family 7 Member 11 (*SLC7A11*), Glutathione Peroxidase 4 (*GPX4*), and Acyl-CoA Synthetase Long Chain Family Member 4 (*ACSL4*). **Conclusion:** Our integrative approach highlights the potential of genomic and immune microenvironment data in developing personalized risk models for BCa, offering insights into individualized treatment strategies. Importantly, *TRIM59* is involved in ferroptosis resistance in BCa. These findings have potential implications for identifying diagnostic biomarkers and therapeutic targets for BCa treatment.

Keywords: BCa; MR; immune; *TRIM59*; biomarkers; ferroptosis

1. Introduction

Bladder cancer (BCa) is one of the most prevalent malignancies affecting the urinary system and is particularly common among men worldwide [1]. The development of BCa is influenced by a combination of environmental and genetic factors, with well-established risk factors including smoking, chronic bladder inflammation, and exposure to certain chemicals, such as aromatic amines [2]. BCa is primarily categorized into two types: non-muscle-invasive bladder cancer (NMIBC) and muscle-invasive bladder cancer (MIBC), with NMIBC accounting for the majority of cases [2]. Early diagnosis and timely intervention are critical for improving patient survival outcomes. Standard treatment modalities include surgical resection, intravesical therapy, radiotherapy, and chemotherapy. Although conventional treatment approaches have demonstrated some effectiveness, the prognosis for advanced-stage BCa, especially in patients with MIBC, remains unsatisfactory, and

the development of more effective therapeutic strategies continues to pose significant clinical challenges [3–5]. The optimal selection and application of immunotherapy regimens remain important clinical challenges that warrant further research [6].

The development of BCa is governed by a range of molecular mechanisms, among which gene mutations, epigenetic modifications, and remodeling of the tumor microenvironment serve as key driving forces [7,8]. Frequently mutated genes in BCa include Tumor Protein P53 (*TP53*), Fibroblast Growth Factor Receptor 3 (*FGFR3*), and RB Transcriptional Corepressor 1 (*RBI*), and alterations in these genes are strongly linked to tumor initiation, progression, and therapeutic response. Notably, *TP53* mutations are recognized as a critical pathogenic event in BCa progression [9]. Furthermore, BCa exhibits distinct epigenetic profiles, such as aberrant DNA methylation and histone modifications, which play a significant role in tumor aggressiveness and patient prognosis [10]. Central to this



process are immune evasion mechanisms, primarily mediated through suppression of T cell activity and the accumulation of immunosuppressive cell populations, including regulatory T cells (Tregs) and myeloid-derived suppressor cells (MDSCs) [11]. High expression levels of immune checkpoint molecules, such as Programmed Cell Death 1 (PD-1) and CD274 Molecule (PD-L1), in BCa cells contribute to immune escape, thereby promoting tumor growth and metastasis. In recent years, immunotherapeutic approaches, particularly PD-1/PD-L1 inhibitors, have demonstrated clinical promise in the treatment of BCa, especially in advanced-stage patients [12]. Previous studies have indicated that increased expression of *SLC7A11* promotes resistance to ferroptosis in BCa by modulating glutathione metabolism. Moreover, research has found that inhibiting *GPX4* can restore sensitivity to chemotherapy in BCa cells that are resistant to ferroptosis. Despite these advances, not all patients exhibit a positive response to immunotherapy, suggesting that the tumor's immunological landscape and its underlying molecular characteristics play a crucial role in determining treatment effectiveness. Consequently, a deeper understanding of the molecular pathways and immune escape mechanisms in BCa is vital for developing more precise, individualized therapies and improving patient outcomes. Through the application of multi-omics approaches, subtype-specific therapeutic targets have been identified in MIBC, with the basal-like subtype showing significant enrichment in genes related to immune checkpoints and ferroptosis.

This study integrates expression quantitative trait loci (eQTL) data with Mendelian randomization (MR) analysis to identify risk genes associated with BCa. Furthermore, a prognostic risk model for BCa is developed using machine learning techniques. Through comprehensive analyses of gene expression and biomarkers, we investigate the relationships between the risk model and BCa subtypes, immune cell infiltration, chemotherapy drug sensitivity, as well as evaluate the model's accuracy and prognostic value. Our findings offer valuable insights that may contribute to more precise classification and tailored treatment strategies for BCa patients.

2. Materials and Methods

2.1 Data Acquisition and Processing

Gene expression and clinical information for BCa were obtained from The Cancer Genome Atlas (TCGA) database (<https://portal.gdc.cancer.gov/>), comprising 412 BCa samples together with their associated clinical details. Furthermore, gene expression profiles and clinical data for an additional 476 cases of urothelial carcinoma (E-MTAB-4321) were also gathered. eQTL data were downloaded from the IEU OpenGWAS initiative (<https://gwas.mrcieu.ac.uk/>), covering a total of 19,942 genes (Supplementary Table 1). Single Nucleotide Polymorphisms (SNPs) with a *p*-value threshold of less than 5

$\times 10^{-6}$ were chosen for subsequent investigation. The genome-wide association study (GWAS) data for BCa were acquired from the FinnGen R11 cohort (<https://www.finnngen.fi/fi>), which consists of 2574 individuals diagnosed with BCa and 345,118 unaffected controls (Supplementary Fig. 1).

2.2 Mendelian Randomization Analysis

This research employed the “TwosampleMR” R package (v0.5.6). To minimize any potential effects of linkage disequilibrium and ensure instrumental variables (IVs) independence, the clustering function was set with parameters $r^2 = 0.1$ and $kb = 10,000$, specifically for European populations. Prior to conducting the MR analysis, palindromic SNPs were removed. For each SNP, Wald ratio estimates were calculated to generate estimates unaffected by confounding factors. Subsequently, a meta-analysis was conducted using several approaches.

2.3 Feature Selection and Risk Model Construction

The R packages ‘survival’ and ‘survminer’ (v4.1-8, v0.4.9) were employed. Univariate Cox regression analysis was conducted using the *coxph* function to pinpoint genes that had a significant impact on the prognosis of BCa patients. These identified genes were then cross-referenced with the eQTL genes obtained from Mendelian randomization analysis, ultimately yielding a refined list of genes used for model construction. Using the selected prognostic features, we built a machine learning-based prognostic model. Machine learning algorithms, including Lasso combined with StepCox, survival-SVM, CoxBoost paired with survival-SVM, Ridge regression, Lasso combined with survival-SVM, and SuperPC, were assessed to determine the most effective model and its corresponding riskScore for predicting patient outcomes. Additional details about the classifiers and algorithms used are provided (Supplementary Table 2).

2.4 Functional Enrichment Analysis

Functional enrichment analysis was conducted using configuration files including “c2.cp.kegg_legacy.v2024.1.Hs.symbols.gmt”, “c5.go.v2024.1.Hs.symbols.gmt”, and “h.all.v2024.1.Hs.symbols.gmt”, implemented through the GSEA function. The ssGSEA enrichment analysis for both groups was carried out utilizing the ‘limma’ (v3.58.1), ‘GSEABase’ (v1.60.0), and ‘GSVA’ (v1.46.0) packages. Pathway ssGSEA scores were calculated using the ‘gsva’ function and subsequently normalized with the ‘normalize’ function. To delve deeper into the association between sample riskScores and pathway ssGSEA scores, a Spearman correlation analysis was conducted. Additionally, a collection of 12 BCa signature features was assembled, and GSVA analysis was applied to all 412 samples. The results were visualized employing the ‘ggridge’ package.

2.5 Molecular Subtypes of BCa

BCa can be classified into distinct molecular subtypes using various methods, such as Cartes d'Identité des Tumeurs (CIT), Lund, MD Anderson Cancer Center (MDA), TCGA, Baylor, University of North Carolina (UNC), and Consensus [13–18]. In this study, we performed subtype classification of 412 BCa samples using the “ConsensusMIBC” (v1.1.0) and “BLCAsubtyping” (v2.1.1) R packages [19]. The molecular subtypes were subsequently analyzed by comparing different groups.

2.6 Immune Infiltration Estimation in BCa

Specifically, to evaluate immune cell infiltration, we utilized several algorithms including Quantiseq, Timer, Mcp_counter, Xcell, Cibersort, and Epic, which were implemented through the “immunedeconv” (v2.1.0) R package. Additionally, ssGSEA was applied using previously established gene signatures specific to immune cell types [20]. To evaluate tumor purity, the “estimate” R package was used. Additionally, Tumor Immune Dysfunction and Exclusion (TIDE) scores were computed for a cohort of 412 BCa patients using an online platform developed [21]. These scores serve as important indicators of immunotherapy response, with elevated TIDE values suggesting a stronger ability of tumor cells to evade immune detection. Differences in TIDE scores between groups were analyzed using the Wilcoxon rank-sum test (‘wilcox.test’).

2.7 Identification of Genetic Variations

Genetic variation characteristics within the TCGA-BLCA were analyzed by R package ‘maftools’ (v2.18.0). To visualize the genetic alterations, Single Nucleotide Variation (SNV) waterfall plots and gene co-mutation heatmaps were generated.

2.8 Analysis of Drug Sensitivity

Subsequently, a correlation analysis was conducted between drug sensitivity and the riskScore, as the criterion for statistical significance, implemented through the “pRRophetic” R package (v0.5) [22].

2.9 Cell Lines

The BCa cell lines 5637 and EJ were provided by the Tianjin Medical University. The cell cultures were kept in a humidified environment containing 5% carbon dioxide (37 °C). All cell lines were validated by STR profiling and tested negative for mycoplasma.

2.10 WB Assay

Proteins were extracted from cell lysates, and their concentrations measured with a Bicinchoninic Acid Assay (BCA) protein assay kit. Subsequently, 35 µg of protein per sample was subjected to sodium dodecyl sulfate polyacrylamide gel electrophoresis (SDS-PAGE). Protein expression levels were evaluated using primary antibodies target-

ing *TRIM59*, *SLC7A11*, *GPX4*, *ACSL4*, and *GAPDH*, each at a dilution of 1:1000 (Abcam, Waltham, MA, USA). Ultimately, the protein bands were evaluated and converted into digital format using ImageJ software (v154-win-java8, Bethesda, MD, USA).

2.11 MTT Assay

EJ and 5637 cells were transfected using a variety of reagents, including a negative control siRNA, two distinct siRNAs targeting *TRIM59* (siRNA-1 and siRNA-2), an empty vector (Ev), and two wild-type *TRIM59* expression constructs (WT1 and WT2), and then cultured for a period of 48 hours. Following this, around 2500 cells were plated into each well of a 96-well plate and allowed to incubate at 37 °C for a duration of 1 to 4 days. At predetermined time points each day, 30 µL of MTT solution was added to each well, and the plate was further incubated at 37 °C for 2 hours. Once the MTT solution was removed, 150 µL of DMSO was added to each well, followed by an additional incubation period of 15 minutes at 37 °C.

2.12 Wound Healing Assay

BCa cells were cultured in 6-well plates. Following a 24-hour incubation period, a negative control siRNA, siRNA-1 and siRNA-2, Ev, or WT1 and WT2 were introduced into the system. A 10-µL pipette tip was then used to create a linear wound across the center of each well. The cells were subsequently rinsed thoroughly and returned to the incubator for an additional 24 to 72 hours. Images of the cell migration were captured at 0, 24, and 72 hours post-treatment using a microscope.

2.13 Transwell Migration Assay

EJ and 5637 cells were introduced into negative control siRNA, siRNA-1 and siRNA-2, Ev, or WT1 and WT2. Subsequently, 20,000 cell were seeded into transwell inserts and were incubated for 48 hours at 37 °C under standard culture conditions. After incubation, the chambers were rinsed twice with PBS. The cells fixed with paraformaldehyde, followed by two additional PBS washes.

2.14 Xenograft Mouse Model

Female BALB/c nude (immunocompromised) mice were used in the study. The animals were 6–8 weeks old and weighed 18–22 g. The injection was administered subcutaneously on the right lower abdominal side. The injection volume was adjusted to 100 µL, with a 1:1 ratio of Matrigel to medium, which included 2×10^6 EJ cells. Tumor volume was calculated using the formula: $V = (\text{length} \times \text{width}^2)/2$, where length refers to the longest diameter and width refers to the shortest diameter perpendicular to the length. For the experimental design: (a) The groups comprised sh control, sh control with JKE-1647/atezolizumab treatment, and sh control with atezolizumab treatment (**Supplementary Fig. 2**). (b) The groups included sh control, sh control with JKE-

1647 treatment, sh *TRIM59*, and sh *TRIM59* treated with both JKE-1647 and atezolizumab. Tumor growth was monitored daily for a minimum of two weeks. The mice were euthanized using conventional cervical dislocation.

3. Results

3.1 Identification of Genes Associated With BCa Using eQTL MR Analysis

A total of 19,942 genes were examined using eQTL analysis, with significant eQTLs identified through *p*-value thresholding and clumping techniques. Following this, F-statistics-based filtering and ID conversion were employed, resulting in the retention of 15,307 eQTLs, which included gene names, and 52,674 SNPs, providing comprehensive coverage of the genome (**Supplementary Table 2**). Subsequently, each eQTL-associated SNP was compared to BCa GWAS data, yielding a final set of 49,823 SNPs. All retained SNPs demonstrated strong instrument validity with F-statistics exceeding 10. A total of 15,035 genes were included in the MR analysis (**Supplementary Table 3**). A total of 313 genes were found to be significantly associated with BCa based on Inverse-Variance Weighted (IVW) analysis. Among these genes, 170 were linked to a higher risk of BCa ($OR > 1$), whereas 143 were linked to a lower risk ($OR < 1$) (Table 1, **Supplementary Tables 4,5**).

3.2 Candidate Gene Identification and Machine Learning Model Development

Using univariate Cox regression analysis, we examined the association between TCGA BCa RNA expression and patient prognosis, identifying 5331 prognostically relevant genes (**Supplementary Table 6**). By intersecting the hazard ratios (HR) and odds ratios (OR) of risk genes derived from both uncox and MR analyses, we identified 34 genes significantly linked to BCa. Among these, 24 were classified as high-risk genes, while 10 were protective genes for BCa (Fig. 1A,B, **Supplementary Table 7**). The genomic locations of these 34 genes are depicted in a chromosomal circular plot (Fig. 1C). MR analysis suggested that the eQTLs of these genes may be significantly associated with BCa prognosis (Fig. 1D). We conducted machine learning analysis on gene expression data from the TCGA and E-MTAB-4321 datasets, employing 101 algorithms to build predictive models and score each sample across all methods (**Supplementary Tables 8,9**). Model validation using the concordance index (C-index) demonstrated that the plsRcox method attained the highest C-index value (Fig. 1E).

3.3 Risk Model Validation

The plsRcox-derived model was selected as our predictive model. Patients in the TCGA cohort were classified into low-risk and high-risk groups based on the optimal cut-off value of the riskScore. The survival outcomes for patients in the high-risk group were notably worse compared

to those in the low-risk group (Fig. 2A, **Supplementary Table 10**). The clinical risk model incorporated variables such as pathological stage, gender, and age. Its predictive performance was evaluated through ROC curve analysis, which demonstrated that the riskScore exhibited greater predictive accuracy compared to conventional clinical indicators, including pathological stage (Fig. 2B). Furthermore, the riskScore demonstrated effectiveness in forecasting patient probabilities at 1-year, 3-year, and 5-year intervals (Fig. 2C). The Concordance Index (C-index) was further utilized to assess the model's predictive performance, confirming that the riskScore offers reliable and consistent survival predictions (Fig. 2D). When validated using the E-MTAB-4321 dataset, the high-risk group again exhibited significantly poorer survival outcomes than the low-risk group (Fig. 2E, **Supplementary Table 10**). Additionally, riskScore showed excellent predictive performance in the E-MTAB-4321 cohort (Fig. 2F–H). Univariate analysis of age, gender, pathological stage, and riskScore confirmed that plsRcox effectively distinguishes between patients with different prognoses (Fig. 2I,K). Multivariate regression analysis, adjusted for age, gender, and pathological stage, confirmed that riskScore significantly predicts patient survival ($HR > 2$) (Fig. 2J,L).

3.4 Various Signaling Pathways in Different Groups

Through various gene expression analyses, we identify the molecular characteristics that differentiate the two groups (high-risk and low-risk group). In high-risk group, Gene Ontology (GO) analysis revealed that critical tumor-related pathways, negative regulation of the canonical Wntless/Integrated (*WNT*) signaling pathway and positive regulation of G protein-coupled receptor signaling pathway. Additionally, pathways linked to tumor development, cell-cell adhesion mediator activity was also more prominent in this group. Conversely, in low-risk group, metabolic processes such as arachidonic acid, estrogen, and uronic acid are enriched. When examining immune-related pathways, in high-risk group, we found that fibroblast-associated functions, like response to fibroblast growth factor were more common. In low-risk group, T-cell-related pathways, T cell receptor complex were predominantly enriched (Fig. 3A). The Kyoto Encyclopedia of Genes and Genomes (KEGG) analysis corroborated the findings from the GO analysis, in low-risk group, showing significant enrichment of metabolic pathways like linoleic acid and ascorbate and aldarate. In contrast, pathways associated with tumor progression, including focal adhesion, cell cycle, and mismatch repair, were more prevalent in high-risk group (Fig. 3B, **Supplementary Table 11**). Subsequently, we examined the enrichment of HallMark gene sets between the two groups. Analysis showed that the high-risk group was distinct in showing significant activation of major tumor-associated pathways, for example, epithelial mesenchymal transition (*EMT*), G2/mitosis (*G2M*) check-

Table 1. eQTL GWAS MR Analysis of the top 50 genes in BCa.

Exposure	Outcome	Method	nsnp	OR	p-value
<i>SHROOM4</i>	BCa	IVW	3	2.282725735	0.002874680
<i>IGHG4</i>	BCa	IVW	3	2.212232996	0.007854922
<i>MXD4</i>	BCa	IVW	4	2.211653888	0.001252362
<i>CHD3</i>	BCa	IVW	3	2.177813144	0.002600537
<i>TUBB4B</i>	BCa	IVW	3	2.006432255	0.010138824
<i>ATP6V0C</i>	BCa	IVW	3	1.844112493	0.035992092
<i>SNX13</i>	BCa	IVW	3	1.749801894	0.003751934
<i>CCNDBP1</i>	BCa	IVW	3	1.725627987	0.020568438
<i>ISY1</i>	BCa	IVW	4	1.686991123	0.038477973
<i>ZNF644</i>	BCa	IVW	3	1.679697555	0.044952987
<i>PAFAH1B3</i>	BCa	IVW	3	1.675820497	0.015235574
<i>ADRA2A</i>	BCa	IVW	5	1.668737363	0.007811729
<i>KIRREL3</i>	BCa	IVW	3	1.653559093	0.011245868
<i>ZNF254</i>	BCa	IVW	3	1.628996476	0.030128596
<i>OXSRI</i>	BCa	IVW	5	1.621258359	0.008803783
<i>JUND</i>	BCa	IVW	3	1.595327921	0.020217129
<i>SLC2A3</i>	BCa	IVW	3	1.573354989	0.028600952
<i>EBF1</i>	BCa	IVW	9	1.567697269	0.026571650
<i>DENND2C</i>	BCa	IVW	3	1.529153776	0.005074320
<i>AGPAT1</i>	BCa	IVW	4	1.518592588	0.002107553
<i>SLC12A9</i>	BCa	IVW	4	1.517706490	0.000716704
<i>GPR183</i>	BCa	IVW	4	1.502956961	0.044233749
<i>LIPH</i>	BCa	IVW	5	1.493282379	0.008303005
<i>CAPN5</i>	BCa	IVW	5	1.491629797	0.006488212
<i>MST1</i>	BCa	IVW	4	1.486326594	0.043811420
<i>AKR7A3</i>	BCa	IVW	3	1.464063269	0.029710515
<i>UBALD2</i>	BCa	IVW	3	1.463006629	0.026593285
<i>CFH</i>	BCa	IVW	7	1.430153681	0.025987911
<i>PDGFRB</i>	BCa	IVW	7	1.416422219	0.008498805
<i>LYL1</i>	BCa	IVW	5	1.410700163	0.024353035
<i>CHIT1</i>	BCa	IVW	4	1.410424624	0.004675523
<i>TOR2A</i>	BCa	IVW	3	1.408130191	0.047575015
<i>LRMDA</i>	BCa	IVW	7	1.398522837	0.039392456
<i>TXNDC16</i>	BCa	IVW	3	1.390219142	0.047665048
<i>ZER1</i>	BCa	IVW	5	1.389190778	0.030827892
<i>CCDC117</i>	BCa	IVW	4	1.386048300	0.003798672
<i>TRIM51BP</i>	BCa	IVW	4	1.381350065	0.044375130
<i>ZNF93</i>	BCa	IVW	3	1.359740799	0.047631251
<i>CYP2E1</i>	BCa	IVW	3	1.355640630	0.032567057
<i>RAB11A</i>	BCa	IVW	7	1.346870088	0.030646713
<i>ZNF101</i>	BCa	IVW	3	1.344689384	0.025154497
<i>KIR2DL1</i>	BCa	IVW	4	1.342334528	0.028900689
<i>RIPK3</i>	BCa	IVW	4	1.340880155	0.033160539
<i>GPR108</i>	BCa	IVW	4	1.327089726	0.012373898
<i>B4GALT3</i>	BCa	IVW	13	1.326277866	0.001747056
<i>FAM53C</i>	BCa	IVW	8	1.322251690	0.023944002
<i>LSM8</i>	BCa	IVW	4	1.312782793	0.000018383
<i>HDGF</i>	BCa	IVW	6	1.312375898	0.019868296
<i>ZNF90</i>	BCa	IVW	3	1.310915264	0.044349693
<i>ECHS1</i>	BCa	IVW	3	1.307398168	0.020623222

eQTL, expression quantitative trait loci; GWAS, genome-wide association study; MR, Mendelian randomization; BCa, Bladder cancer; nsnp, number of snps; OR, odds ratio; IVW, Inverse-Variance Weighted.

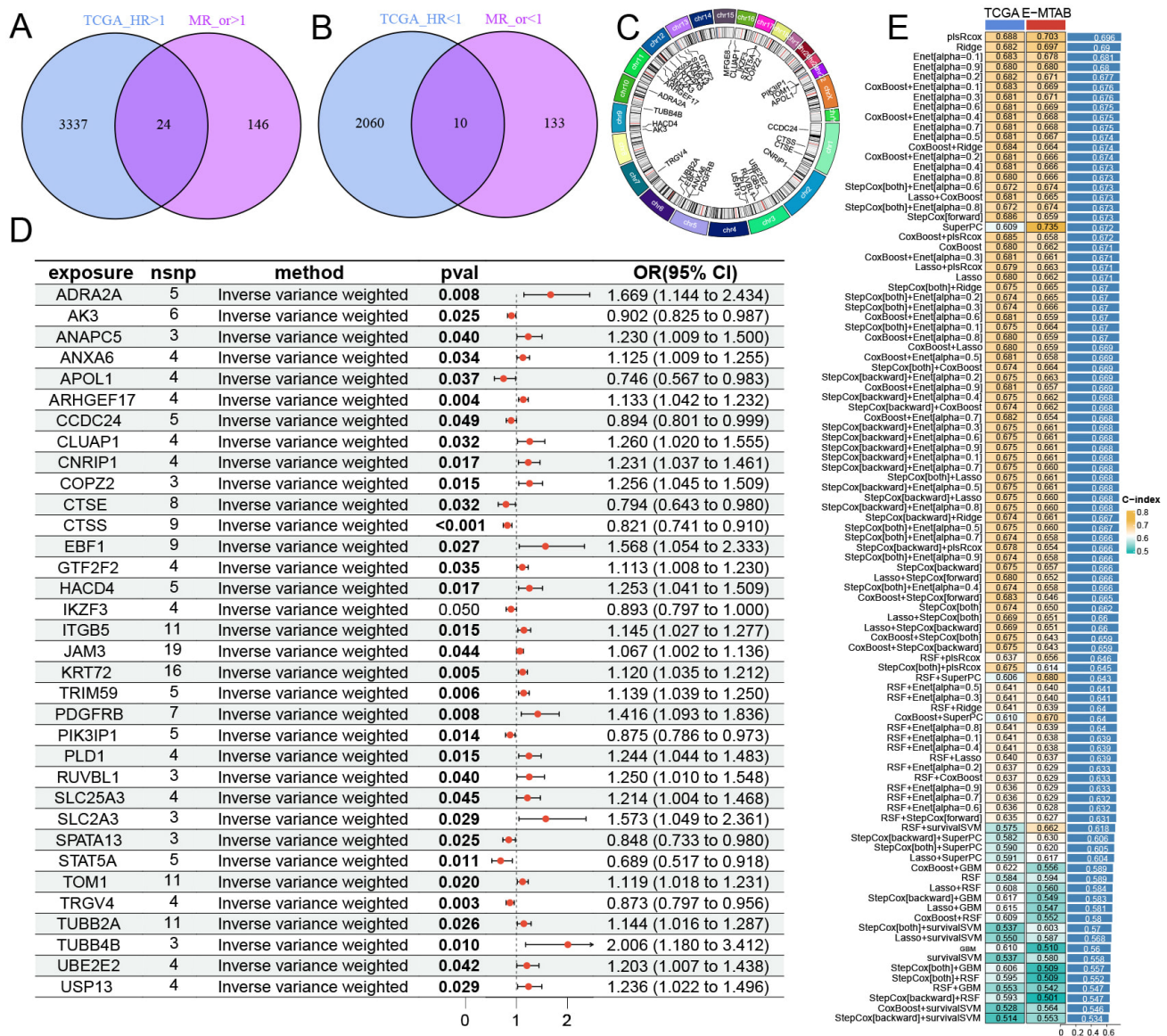


Fig. 1. Candidate gene screening and machine learning model construction. (A,B) Intersection of genes were identified by selecting MR risk genes and unioox prognostic genes. (C) The genomic locations of each feature gene on the chromosome. (D) MR analysis results of eQTL for intersection genes in BCa. (E) Analysis results of intersection genes using 101 machine learning methods in TCGA and E-MTAB-4321.

point, Kirsten rat sarcoma viral oncogene homolog (*KRAS*) signaling down, and E2F transcription factor checkpoint (*E2F*) targets (Fig. 3C, **Supplementary Table 11**). We assembled a collection of BCa differentiation-related genes (**Supplementary Table 12**) and conducted Gene Set Enrichment Analysis (GSEA) to evaluate the molecular features of the two subgroups. In low-risk group, gene sets for luminal differentiation and urothelial differentiation were mainly enriched, whereas in high-risk group, those related to basal differentiation, EMT, myofibroblasts, and additional pathways were enriched (Fig. 3D, **Supplementary Table 13**).

3.5 Molecular Subtypes of High-Risk and Low-Risk Groups

Molecular subtypes and pathological stages were examined to explore the ability of riskScore to distinguish the molecular features of BCa subtypes. There was a greater proportion of patients at stage IV in high-risk group, whereas more individuals at stage II in low-risk group. Moreover, riskScores in stage II cases were markedly lower compared to those in stage IV cases (Fig. 4A,B). In high-risk group, by using the Baylor.subtype classification, we observed a significant prevalence of the Basal subtype (Fig. 4C,D, **Supplementary Table 14**). In low-risk group, by the analysis via the CIT.subtype approach showed that the MC1 subtype was predominantly present. In high-risk

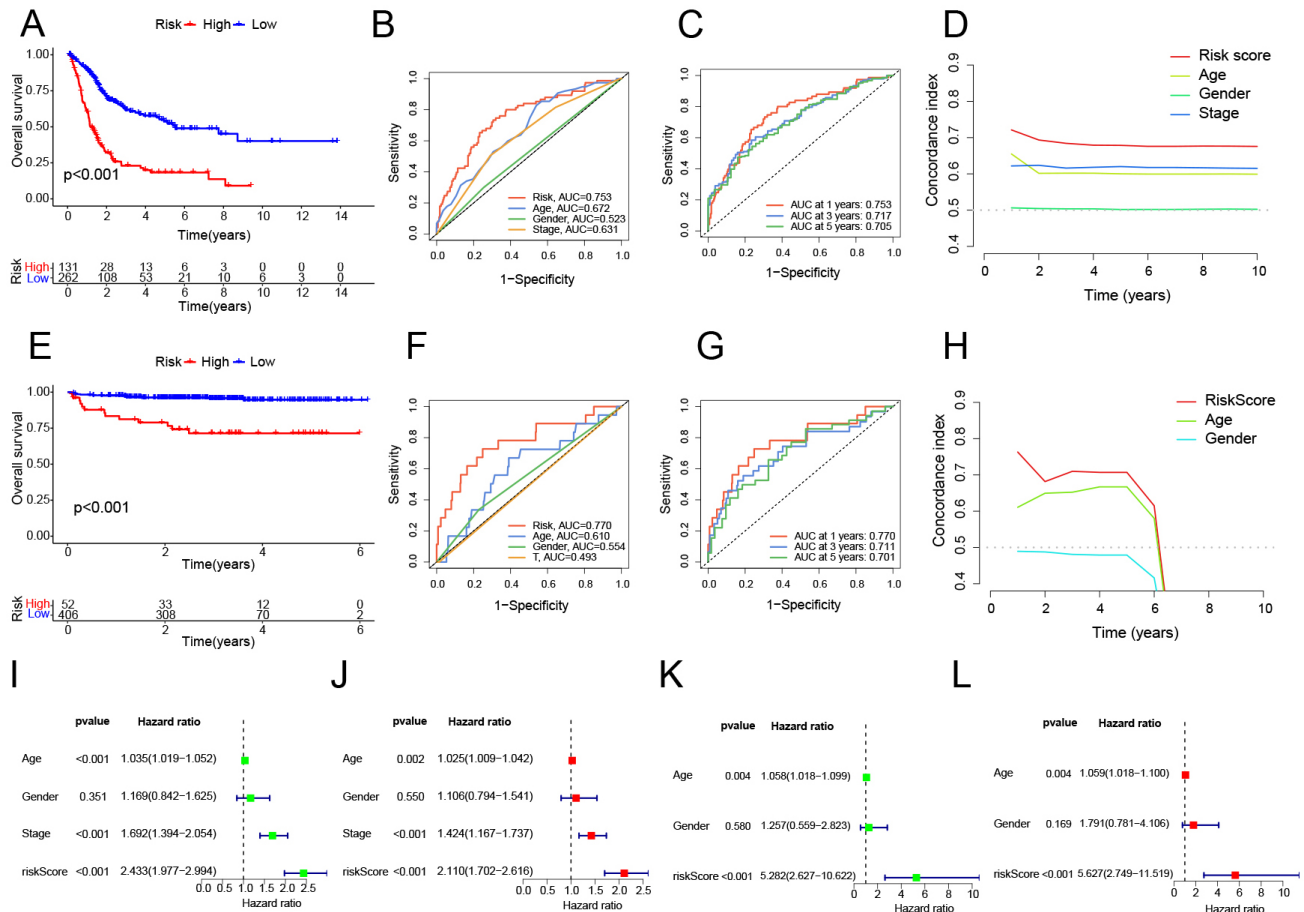


Fig. 2. Survival analysis and accuracy validation using the plsRcox method. (A,E) Survival curves between high-risk and low-risk groups in TCGA and E-MTAB-4321. (B,C,F,G) ROC curves for different clinical indicators and risk models at different time points in TCGA and E-MTAB-4321, with higher AUC values indicating greater predictive accuracy of the model. (D,H) C-index for different clinical indicators and risk models at different time points in TCGA and E-MTAB-4321. (I,K) Univariate Cox analysis of different clinical indicators and risk models in TCGA and E-MTAB-4321. (J,L) Multivariate Cox analysis of different clinical indicators and risk models in TCGA and E-MTAB-4321.

group, the MC7 subtype was mainly observed (Fig. 4E,F, **Supplementary Table 14**). According to the Lund subtype system, the Ba/Sq subtype was primarily linked to high-risk group, whereas in low-risk group, the UroA-Prog subtype was more frequently found (Fig. 4G,H, **Supplementary Table 14**). In high-risk group, MDA subtype, UNC subtype, TCGA subtype, and MIBC subtype classifications, basal-like subtypes were predominantly, while in low-risk group, luminal-like subtypes were more prevalent (Fig. 4I-P, **Supplementary Tables 14,15**). These results indicate that riskScore is effective in distinguishing BCa molecular subtypes. Elevated riskScores are more closely connected with basal-like differentiation, while reduced riskScores show a stronger association with luminal-like differentiation. This observation aligns with previous genomic studies on BCa differentiation.

3.6 Tumor Immune Microenvironment in High-Risk and Low-Risk Groups

Data on immune-related signaling pathways were gathered (**Supplementary Table 16**). Pathway analysis indicated a significant enrichment of immune-related pathways in high-risk group, such as 'Cytokine production immune response', 'Leukocyte migration', 'Regulation of cytokine production', and 'T helper 1 immune response up' (Fig. 5A, **Supplementary Table 17**). The high-risk group in BCa-associated immune pathways showed enrichment in critical BCa pathways, including 'Cell cycle', 'Mismatch repair', 'EMT2', and 'FGFR3-related genes' (Fig. 5B, **Supplementary Table 17**). In high-risk group, analysis of the seven-step tumor immune development process showed the 'Release of cancer cell antigens' pathway was predominant (Fig. 5C, **Supplementary Table 17**). By utilizing multiple immune cell infiltration estimation techniques, such as Estimate, MCPcounter, Timer, Epic, CIBERSORT, and Quantiseq, the extent of immune cell infiltration within each sam-

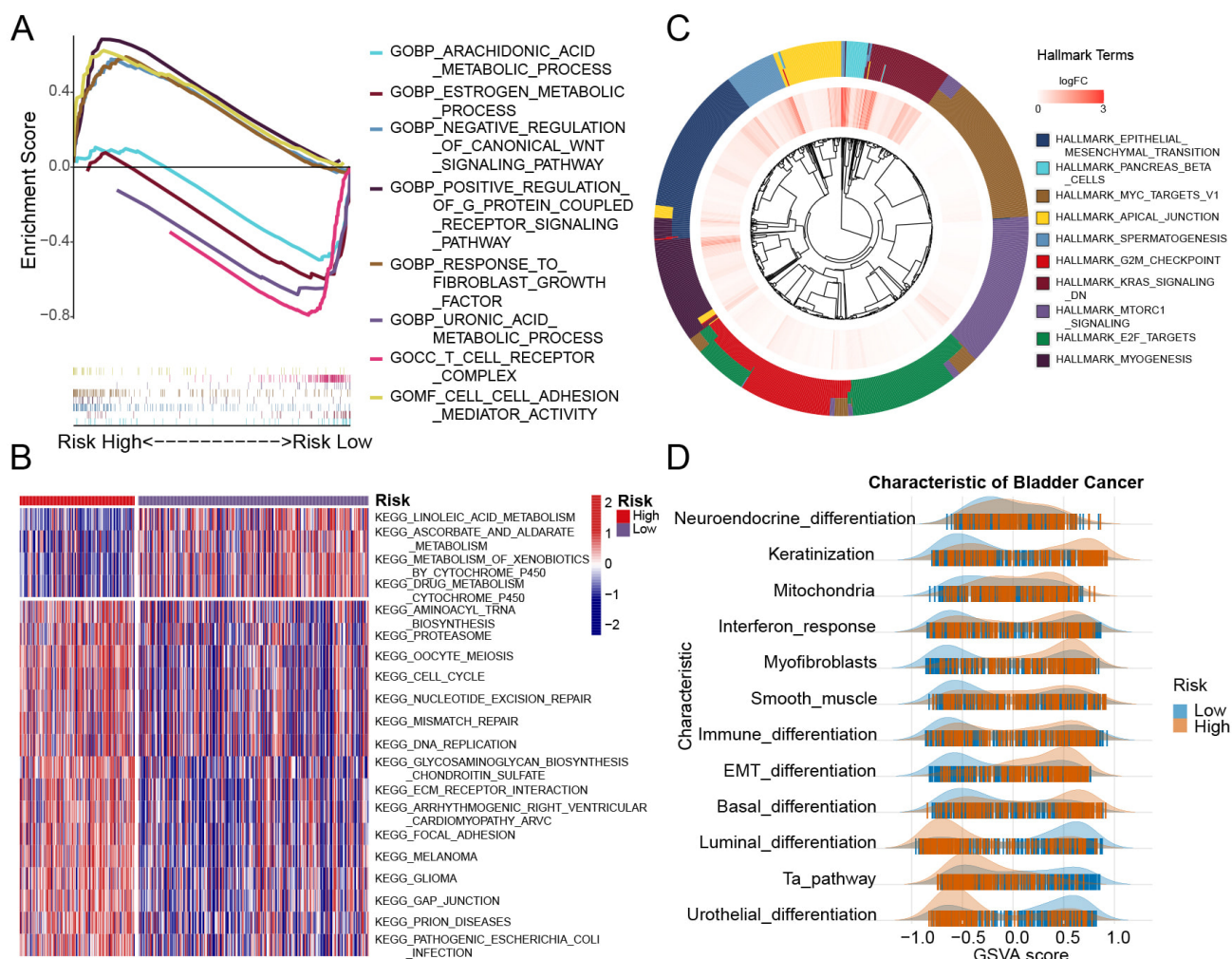


Fig. 3. Gene enrichment analysis results for two group samples. (A) GO enrichment revealed distinct gene enrichment patterns between the high-risk and low-risk groups. The peak on the upper left represents genes enriched in the high-risk group, while the peak on the lower right indicates gene enrichment in the low-risk group. (B) The heatmap displays the enrichment results of various signaling pathways across individual samples in the high-risk and low-risk groups. (C) The outer circle represents the gene characteristics of each signaling pathway, while the inner circle displays the log-fold change (logFC) values of gene expression in the high-risk group compared to the low-risk group. (D) The ridge plot illustrates the distribution of various signaling pathways of BCa characteristic across the samples. GO, Gene Ontology.

ples were showed (Supplementary Table 18). The analysis demonstrated a strong relationship between macrophage infiltration levels and riskScore across the CIBERSORT, Timer, Quantiseq, and Epic methods. The MCPcounter, Xcell, and Epic methods demonstrated a positive correlation between riskScore and fibroblast infiltration, reinforcing the previous finding that ‘response to fibroblast growth factor’ in high-risk group. Furthermore, the CIBERSORT and Xcell methods indicated a positive correlation between riskScore and neutrophil infiltration levels. In the Xcell, CIBERSORT, and Quantiseq methods, a negative relationship was observed between CD8+ T cell infiltration levels and riskScore (Fig. 5D).

3.7 The Analysis of Immune Cell Infiltration and Risk Model

Estimate package indicated that the StromalScore was lower in low-risk group compared to high-risk group (Fig. 6A,B). Subsequently, we conducted ssGSEA analysis on key genes representing 28 different immune cell types (Supplementary Table 19). The results revealed a negative association between CD4 T cells and CD8 T cells (Fig. 6C, Supplementary Table 20). Analysis using the TIDE website (Supplementary Table 21) indicated a strong connection in riskScore, MDSCs and cancer-associated fibroblasts (CAF) (Fig. 6D). Additionally, a positive correlation between riskScore and both TIDE and Exclusion scores (Fig. 6D) indicates that elevated riskScores are linked to greater immune escape potential, potentially

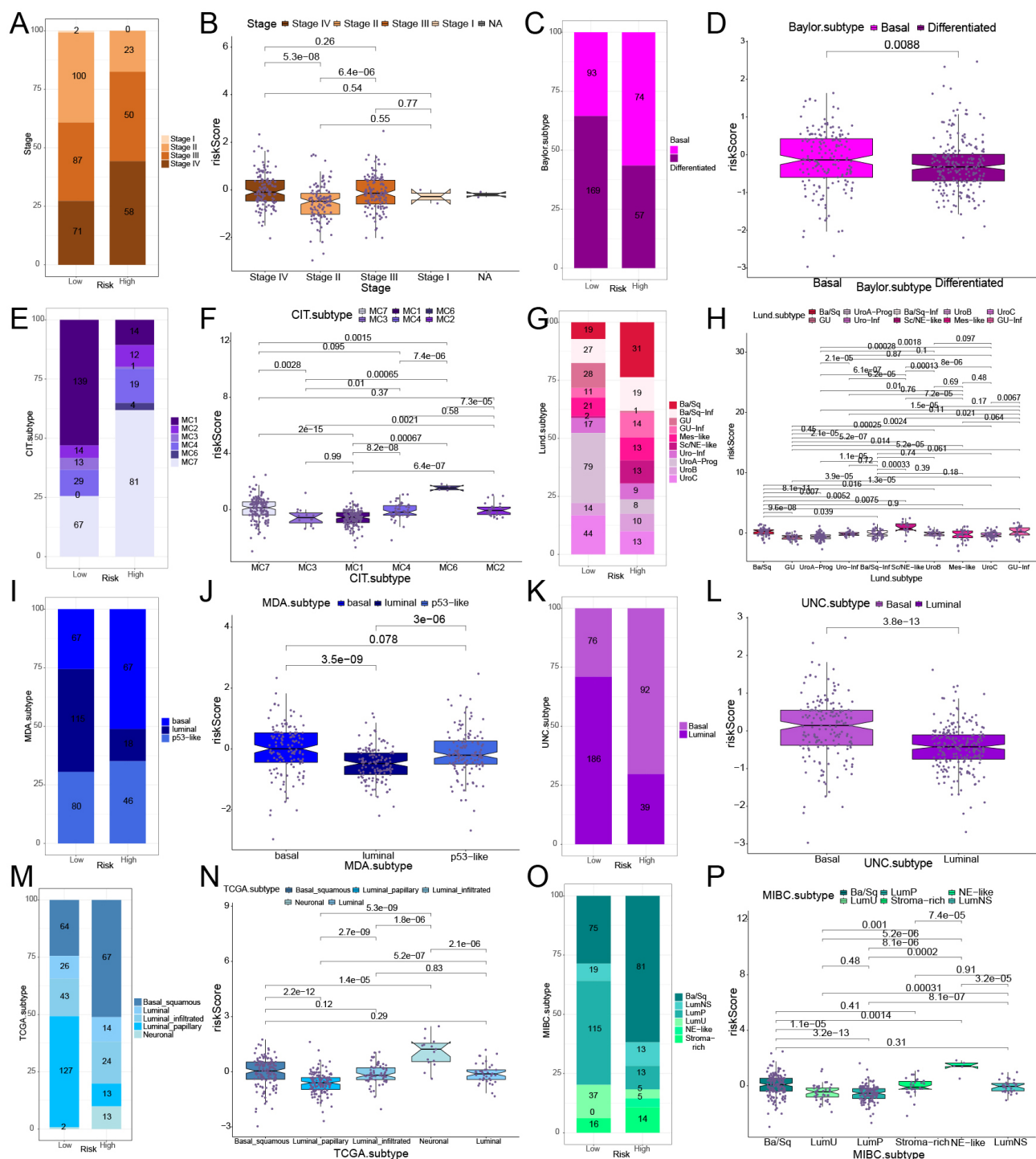


Fig. 4. Relationship between various molecular subtypes and risk model of BCa in the TCGA BCa cohort. (A,C,E,G,I,K,M,O) The distribution and proportion of molecular subtypes and stages of BCa in two groups, based on various classification methods. (B,D,F,H,J,L,N,P) The correlation analysis between BCa molecular subtypes and stages with riskScore in two groups, based on various classification methods.

forecasting less favorable outcomes in immune checkpoint inhibitor (ICI) therapies. Further investigation into immune checkpoints suggested potential differences in the effectiveness of immunotherapy. Specifically, Tumor necrosis factor receptor superfamily member 14 (*TNFRSF14*) showed markedly reduced expression in the high-risk group, while

Tumor Necrosis Factor Ligand Superfamily Member 9 (*TNFSF9*), Tumor necrosis factor receptor superfamily member 18 (*TNFRSF18*), and *CD209* were expressed at lower levels in the low-risk group (Fig. 6E). In contrast, the high-risk group exhibited significantly increased expression of the co-inhibitory immune checkpoints *CD276*, Signal-

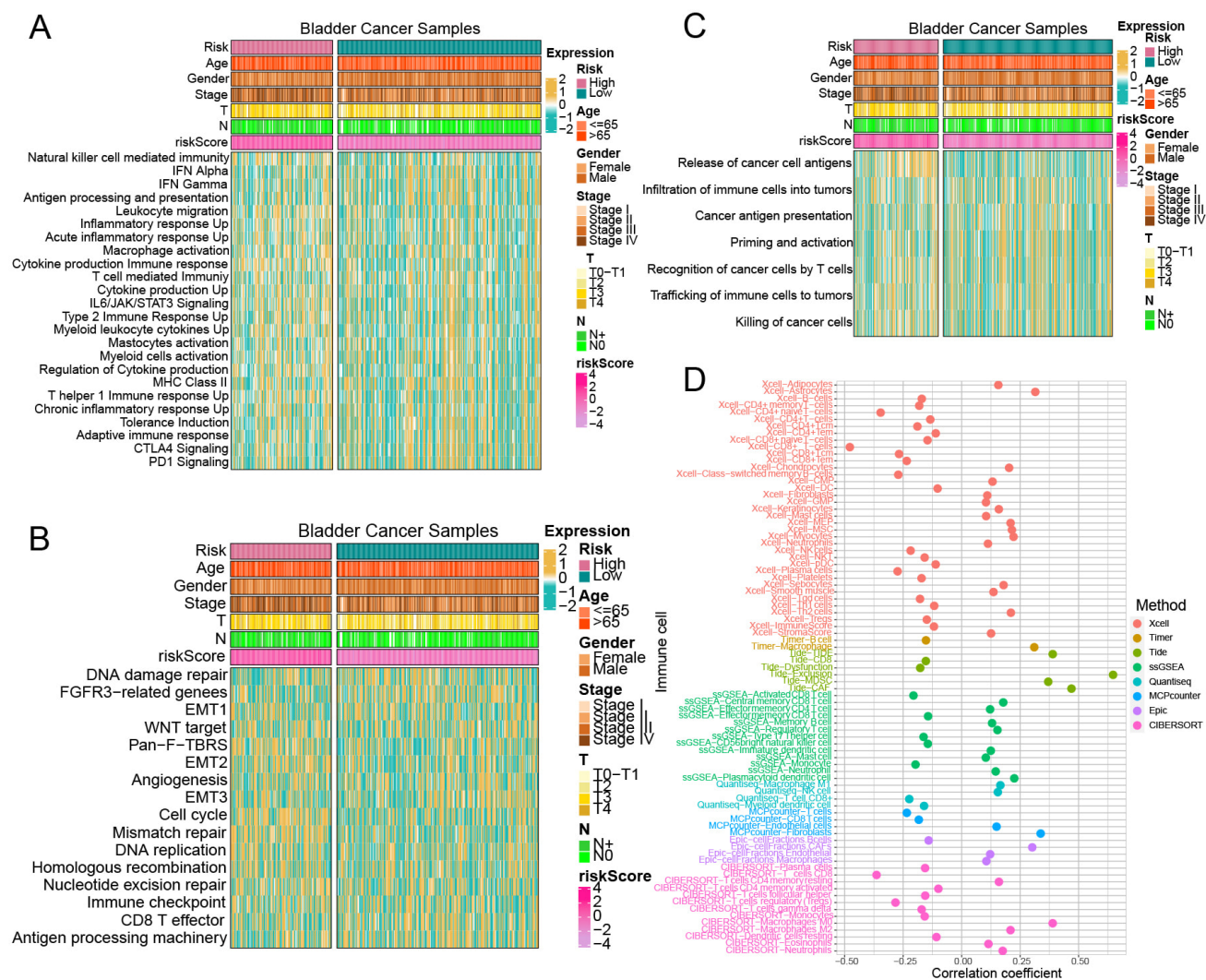


Fig. 5. The relationship between the risk model and immune pathway enrichment levels, immune cell infiltration levels. (A–C) Immune-related pathway enrichment levels between high-risk and low-risk groups. (D) Correlation between riskScore and immune cell infiltration levels across various immune cell estimation methods.

regulatory Protein Alpha (*SIRPA*), and PVR Cell Adhesion Molecule (*PVR*). Meanwhile, low-risk group demonstrated higher expression levels of Galectin 9 (*LGALS9*), Carcinoembryonic Antigen Related Cell Adhesion Molecule 1 (*CEACAM1*), and *CD96* (Fig. 6F). The analysis revealed a significant inverse relationship between TMB and the riskScore, as high-risk group displayed considerably lower level of TMB (Fig. 6G,H). Sankey plot indicated that high-risk group had a reduced presence of T cells and cytotoxic T lymphocytes, suggesting a potential decrease in the effectiveness of ICI therapies for these patients (Fig. 6I).

3.8 Characteristics of Genetic Mutations in Groups With Different Risk Levels

To investigate variations in genetic mutation patterns between high-risk and low-risk groups, we analyzed data from TCGA. Our findings revealed distinct differences in the mutation rates of three key genes—*TP53*,

Titin (*TTN*), and Phosphatidylinositol-4,5-bisphosphate 3-kinase catalytic subunit alpha (*PIK3CA*)—across the two groups. In particular, high-risk group was frequently associated with mutations in *TP53*, while mutations in *TTN* and *PIK3CA* were more commonly observed in low-risk group (Fig. 7A,B). Co-mutation analysis further uncovered groups. In high-risk group, *TP53* mutations frequently co-occurred with those in *TTN* and Lysine-specific demethylase 6A (*KDM6A*), by contrast, *TP53* tended to co-mutate with FAT atypical cadherin 4 (*FAT4*) and spectrin repeat containing, nuclear envelope 1 (*SYNE1*) in low-risk group (Fig. 7C,D). A key observation was that *PIK3CA* showed no significant co-mutation or mutual exclusivity with other genes in high-risk group, but in low-risk group, it commonly co-mutated with *TTN*, *KDM6A*, ryanodine receptor 2 (*RYR2*), and AHNAK Nucleoprotein (*AHNAK*) (Fig. 7C,D). To gain deeper insights into the clonal properties of mutations across the two groups, we performed

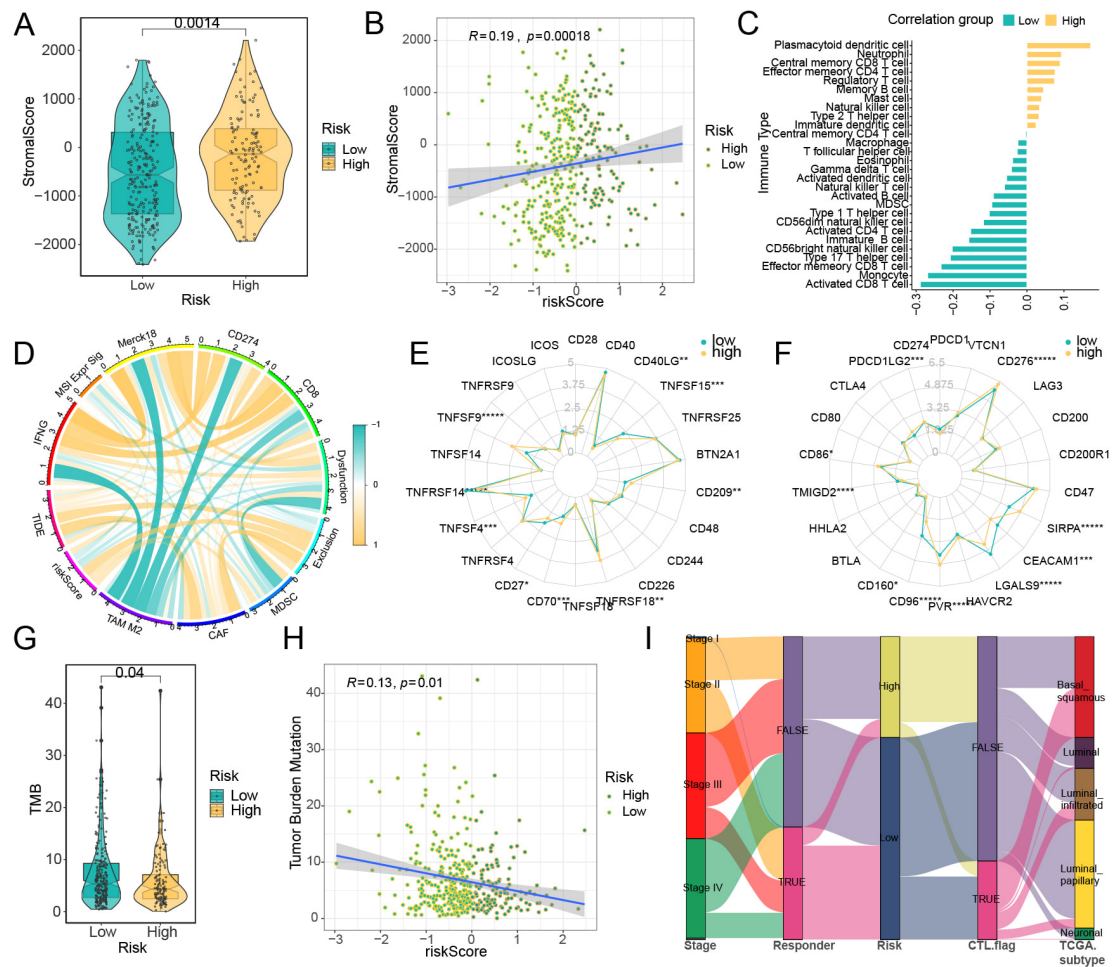


Fig. 6. Correlation analysis between immune cell infiltration levels and risk model. Analysis results of the ESTIMATE method in TCGA samples: (A) The results of stromalScore between high-risk and low-risk groups. (B) The results of correlation between riskScore and stromalScore. (C) The correlation between riskScore and the levels of tumor immune cell infiltration, with yellow representing a positive correlation and blue-green representing a negative correlation. (D) The correlation between riskScore and various TIDE prediction indicators, with yellow lines representing positive correlations and blue-green lines representing negative correlations. (E) Co-stimulatory immune checkpoints, (F) Co-inhibitory immune checkpoints. The relationship between the risk model and tumor mutational burden (TMB) in BCa: (G) Variations in TMB levels between two cohorts; (H) Association analysis between TMB and riskScore. (I) A Sankey diagram depicting the immune profiles of samples in two groups based on TIDE assessment. * $p < 0.05$, ** $p < 0.01$, *** $p < 0.001$, **** $p < 0.0001$, ***** $p < 0.00001$.

variant allele frequency (VAF) analysis. High-risk group showed a significantly lower average VAF compared to low-risk group. *TTN*, *TP53*, and *MUCIN 16*, *CELL SURFACE ASSOCIATED (MUC16)* ranked as the top three genes with the highest average VAF in both groups; however, in low-risk group, their VAF values were substantially higher (Fig. 7E,F). Collectively, these results showed the RiskScore can effectively distinguish the genetic mutation profiles of high-risk and low-risk groups.

3.9 *TRIM59* Is Related to the Ferroptosis Metabolic Pathway, and It has Certain Predictive Ability for the Therapeutic Effect of PD-L1

The Hallmark pathway enrichment analysis revealed that oxidative phosphorylation and peroxisome plays a reg-

ulatory role in ferroptosis (Fig. 8A). The GO pathway enrichment analysis indicated that “OXIDOREDUCTASE_ACTIVITY_ACTING_ON_A_HEME_GROUP_OF_DONORS” are associated with ferroptosis, exhibiting negative correlations (Fig. 8B). The KEGG pathway enrichment analysis also indicated that the high-expression *TRIM59* group was enriched in signaling pathways closely related to ferroptosis, such as Peroxisome, Proteasome, Citrate Cycle TCA Cycle, and Fatty Acid Metabolism (Fig. 8C). Pathway enrichment analysis identified *TRIM59* as being associated with multiple ferroptosis-related signaling pathways. Additionally, the correlation between *TRIM59* and various metabolic genes was examined. Notably, *TRIM59* exhibited strong correlations with key ferroptosis-related

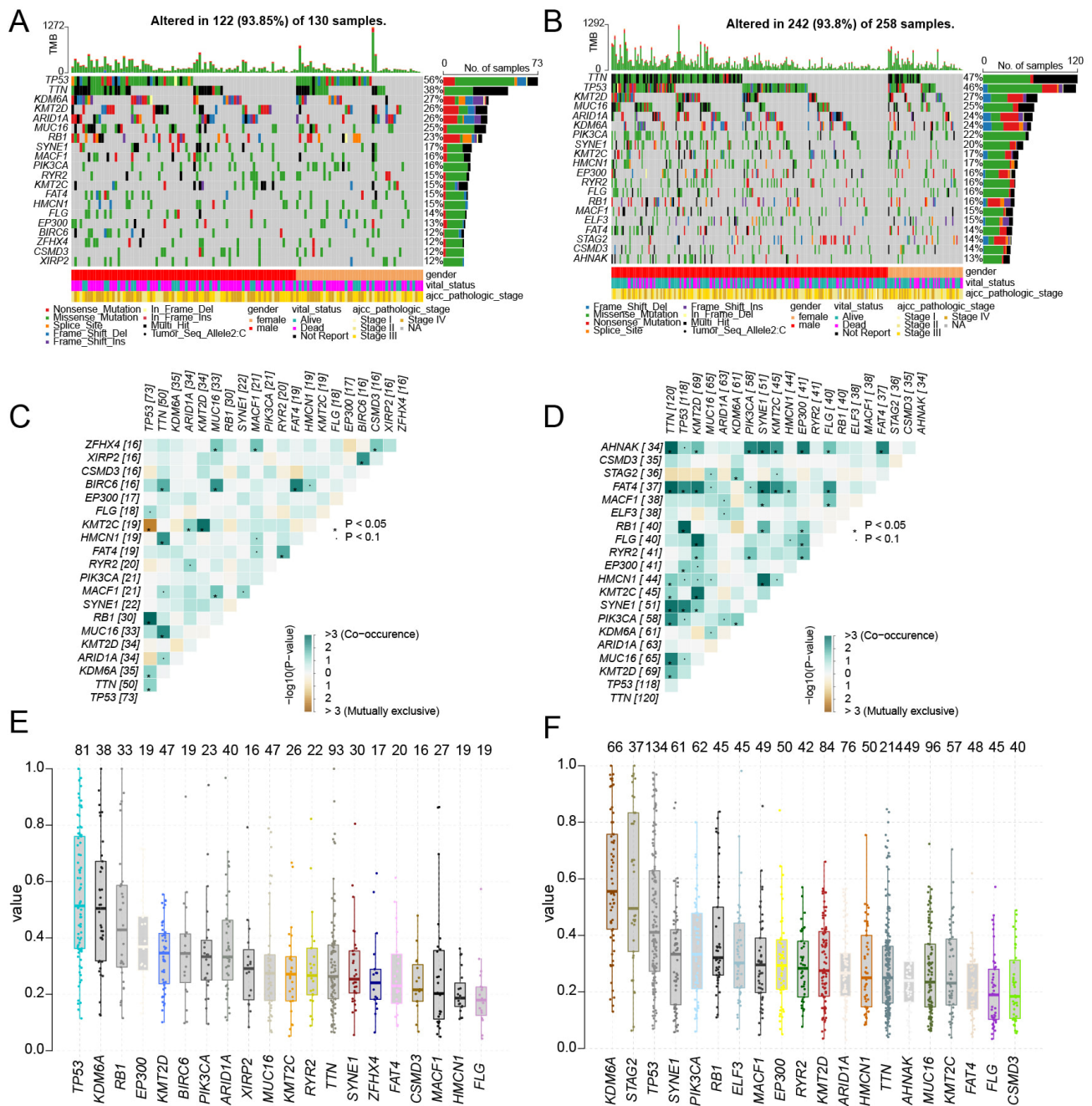


Fig. 7. Gene mutation characteristics of high and low risk groups. ((A) high risk group, (B) low risk group) The waterfall plot illustrates the top 20 gene mutation characteristics and TMB status in two groups. ((C) High risk group, (D) low risk group) The mutation heatmap displays the co-mutation and co-exclusion patterns of the top 20 genes between the high-risk and low-risk groups. ((E) high risk group, (F) low risk group) The boxplot illustrates the differences in the average VAFs between the high-risk and low-risk groups.

genes (*SLC7A11*, *GPX4*, *ACSL4*) and peroxisomal genes (nitric oxide synthase 2 (*NOS2*), superoxide dismutase 2 (*SOD2*), Isocitrate Dehydrogenase 1 (*IDH1*)) (Fig. 8D). In the IMVigor210 dataset, although there was no significant survival difference between the high and low expression groups of *TRIM59*, the grouping based on the levels of TMB and *TRIM59* could clearly distinguish the prognosis of BCa patients undergoing immunotherapy (Supplementary Fig. 3A,B). By analyzing the expression level of *TRIM59* and

the response effect of immunotherapy, it was found that the proportion of patients with stable disease (SD) in the *TRIM59* low-expression group was higher than that in the *TRIM59* high-expression group. Although the expression level of *TRIM59* cannot completely distinguish between patients with a complete response (CR) and those with SD, since its p -value ($p = 0.073$) is close to 0.05, it still has some reference value (Supplementary Fig. 3C,D). And the expression level of *TRIM59* in the IC2+ group was

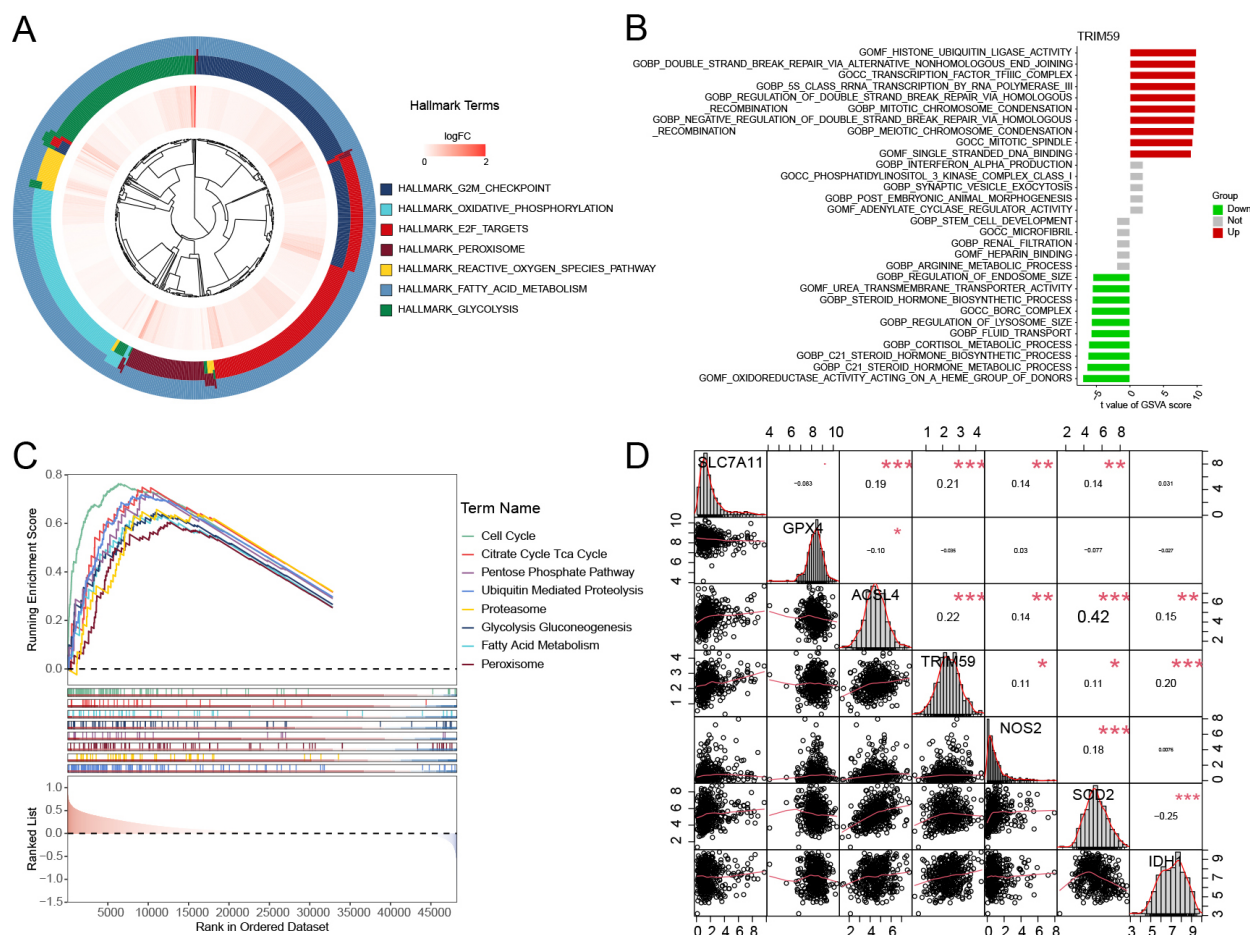


Fig. 8. Hallmark, GO, and KEGG enrichment pathway analysis of *TRIM59* in distinct BCa groups. (A) Hallmark enrichment pathway analysis of *TRIM59*. (B) GO enrichment pathway analysis of *TRIM59*. (C) KEGG enrichment pathway analysis of *TRIM59*. (D) The correlation between *TRIM59* and ferroptosis key genes (*SLC7A11*, *GPX4*, *ACSL4*) and peroxisome genes (*NOS2*, *SOD2*, *IDH1*). KEGG, Kyoto Encyclopedia of Genes and Genomes. * $p < 0.05$, ** $p < 0.01$, *** $p < 0.001$.

significantly higher than that in the IC0 group of patients (Supplementary Fig. 3E,F). In the IMVigor210 data analysis, it was demonstrated that *TRIM59* has the potential to predict the therapeutic effect of PD-L1 treatment.

3.10 *TRIM59* Is Positively Correlated With the Progression of BCa and Enhances the Viability of BCa Cells When Exposed to Doxorubicin (DOX)

Then, we selected *TRIM59* among the 34 genes for further experimental investigation. In Fig. 9A,B, we observed an over-expression of *TRIM59* in 8 BCa tissues compared to matched non-tumor tissues. Additionally, to evaluate the clinical significance of *TRIM59*, we performed immunohistochemistry (IHC) experiments on samples from 16 patients. The results revealed that the average positive region of *TRIM59* in normal tissues was 16%, whereas it increased to 50% in tumor tissues (Fig. 9C,D). Knockdown of *TRIM59* increased the inhibitory impact of DOX on cell proliferation (Fig. 9E,F), suggesting a positive correlation between *TRIM59* expression and the viability of BCa cells treated with DOX.

3.11 *TRIM59* Influences BCa Cell Proliferation, Migration, and Invasion by Promoting Ferroptosis When Knocked Down and Reducing Ferroptosis When Overexpressed

We examined the effects of *TRIM59* siRNA (si#1 and si#2) on ferroptosis in EJ cells and transfected 5637 cells with a lentivirus to overexpress *TRIM59*. MTT, invasion, and wound healing assays indicated that *TRIM59* knock-down decreased EJ cell proliferation, migration, and invasion (Fig. 10A,C,E). In contrast, *TRIM59* overexpression increased the proliferation, migration, and invasion of 5637 cells (Fig. 10B,D,F). Importantly, *TRIM59* siRNA down-regulated the protein levels of key ferroptosis repressors, including *TRIM59*, *GPX4*, and *SLC7A11*, while inducing *ACSL4* expression in EJ cells (Fig. 10G–K). *TRIM59* overexpression elevated the protein levels of *TRIM59*, *GPX4*, and *SLC7A11*, while reducing *ACSL4* protein levels (Fig. 10L–P). Similar results were observed at the RNA level of ferroptosis-related markers (Fig. 10Q,R). To examine how *TRIM59* influences ferroptosis-related genes, we initially explored the potential interaction between *TRIM59*

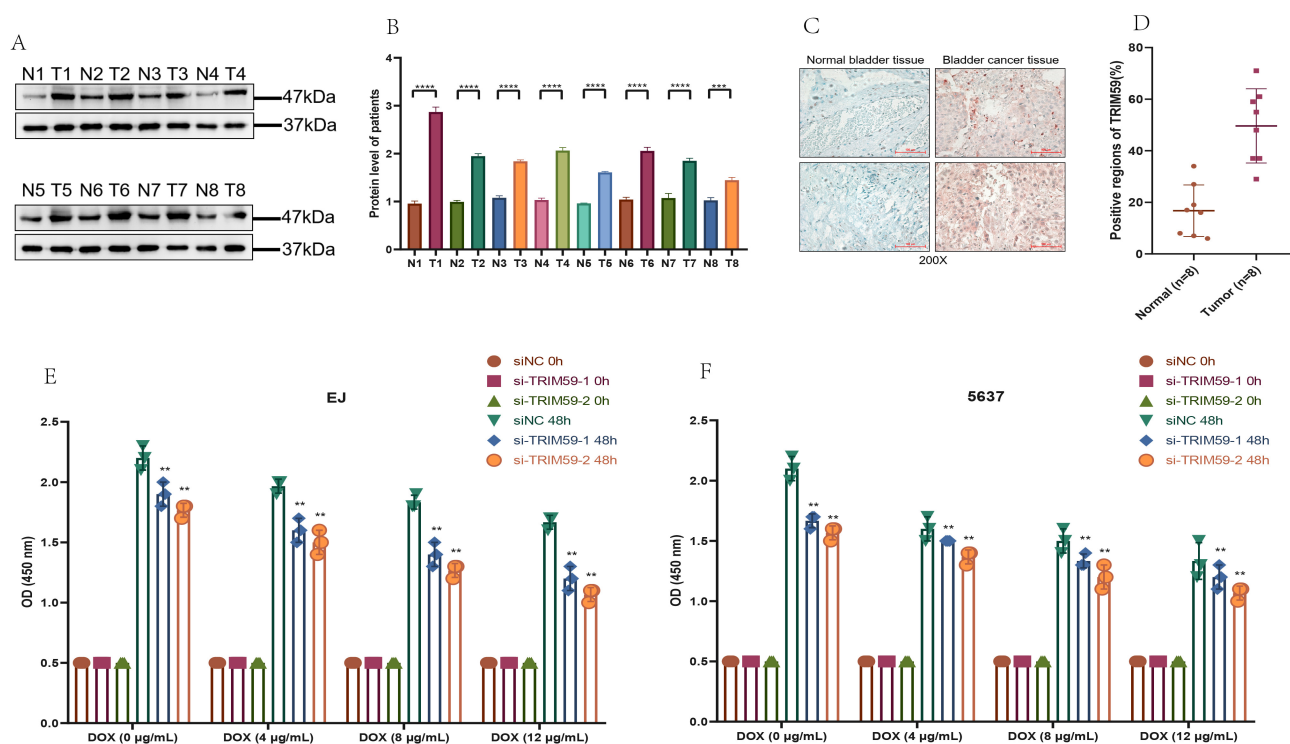


Fig. 9. *TRIM59* expression of BCa patients and impact of *TRIM59* on BCa cell proliferation under DOX exposure. (A) WB assay to examine the *TRIM59* protein expression in BCa tissues. (B) Quantification of (A). (C) IHC assay to examine the *TRIM59* protein expression in BCa tissues (Scale bar = 100 μ m). (D) Quantification of (C). *TRIM59* knockdown inhibits the proliferation of EJ (E) and 5637 (F) cells exposed to DOX. ** $p < 0.01$, *** $p < 0.001$, **** $p < 0.0001$.

and ACSL4, considering that E3 ubiquitin ligases typically exert their function by binding to target substrates. Co-immunoprecipitation (IP) experiments confirmed a direct association between *TRIM59* and ACSL4 (**Supplementary Fig. 4A**).

To determine whether ACSL4 is subject to regulation through the ubiquitin-proteasome system, EJ cells were exposed to MG132, a proteasome inhibitor, and ACSL4 protein levels were assessed at various time intervals using WB. The results demonstrated a progressive accumulation of ACSL4 protein over time (**Supplementary Fig. 4B**), suggesting that ACSL4 is likely regulated via this pathway. To further validate this regulatory mechanism, *TRIM59*-knockdown EJ cells were transfected with wild-type ubiquitin plasmids and subsequently treated with MG132 for 8 hours. Analysis of ACSL4 ubiquitination levels revealed a marked reduction in ubiquitination when *TRIM59* expression was suppressed (**Supplementary Fig. 4C**). In contrast, 5637 cells were transfected with both *TRIM59* overexpression plasmids and wild-type ubiquitin plasmids, followed by MG132 treatment for 8 hours. Western blot results indicated a significant increase in ACSL4 ubiquitination corresponding to elevated *TRIM59* expression (**Supplementary Fig. 4D**). To assess the impact of *TRIM59* inhibitors on BCa cells, three compounds (CID123456, CID789012, and CID345678) were tested. MTT assays

identified CID123456 as the most effective inhibitor, capable of suppressing the proliferation of both EJ and 5637 cells with half-maximal inhibitory concentrations (IC_{50}) of 12.5 μ M and 15.3 μ M, respectively (**Supplementary Fig. 4E,F**). Collectively, these findings indicate that upregulation of *TRIM59* mitigates ferroptosis in BCa cells.

3.12 Determination of the Effect of *TRIM59* on the Level of Ferroptosis of BCa Cells and Effect of JKE-1647/atezolizumab on the Growth of Subcutaneous Transplanted Tumors in Nude Mice

To validate the effect of ferroptosis on BCa cells, we treated cells with the ferroptosis activator (1S,3R)-RSL3 (*RSL3*) and the ferroptosis inhibitors ferrostatin-1 and deferoxamine (iron chelator). Activation of the ferroptosis pathway significantly reduced cell viability in three BCa cell lines, and this effect was reversed by ferroptosis inhibitors (Fig. 11A,E), indicating that activation of the ferroptosis pathway decreases BCa cell viability. In EJ and 5637 cells with *TRIM59* knockdown or overexpression, *RSL3* treatment at varying concentrations for 24 hours showed that the IC_{50} of *RSL3* decreased with *TRIM59* knockdown and increased with overexpression. Cells treated with *RSL3* showed reduced viability in si-*TRIM59*, *TRIM59* OE groups compared to controls (Fig. 11B,C,F,G). Lipid peroxidation levels increased in *TRIM59* knockdown groups and decreased in overexpression groups following

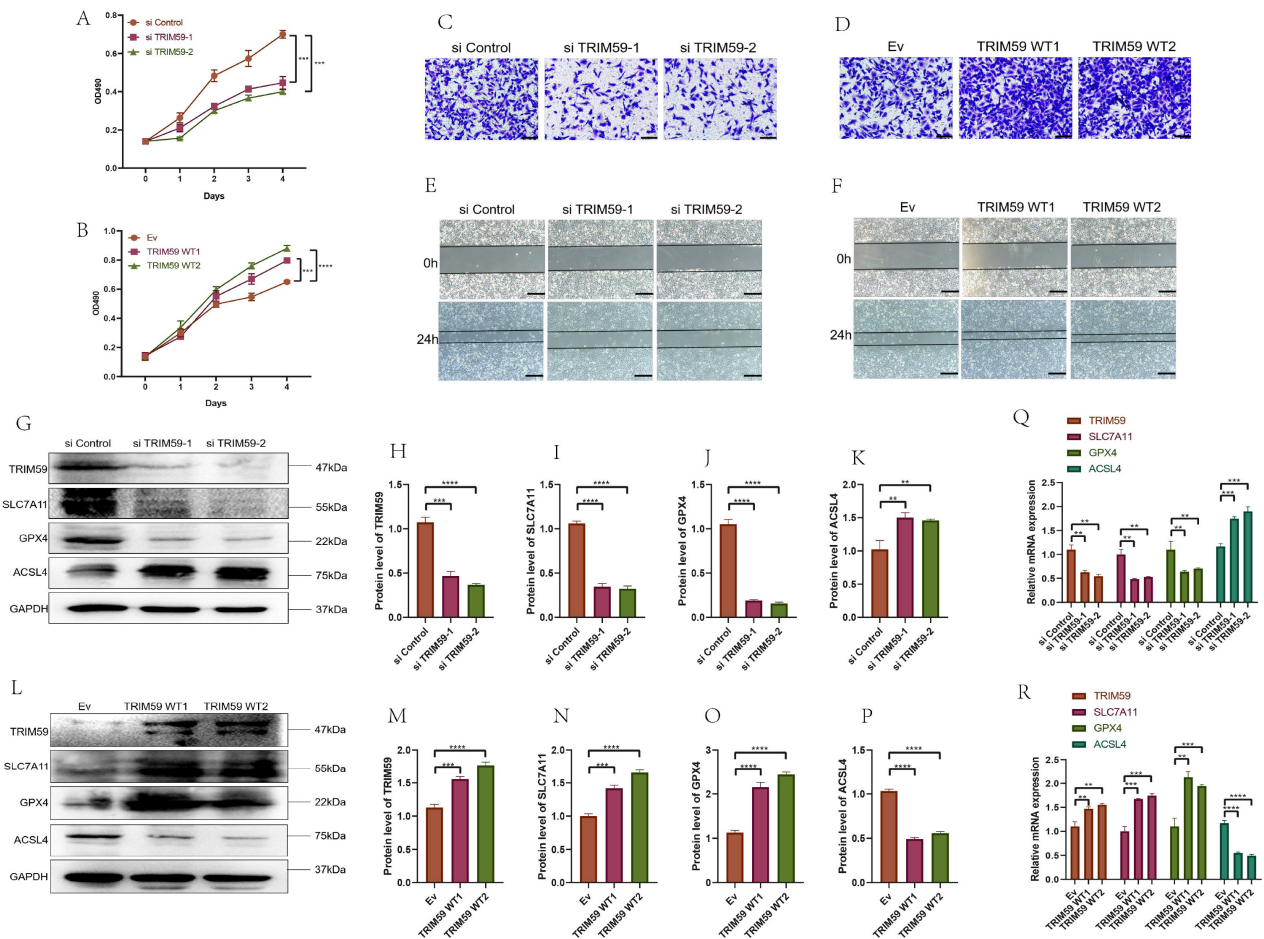


Fig. 10. *TRIM59* affect BCa cell proliferation, migration, and invasion and enhanced ferroptosis through *TRIM59* knockdown in BCa cells and attenuated ferroptosis via *TRIM59* overexpression in BCa. (A) MTT test after *TRIM59* knockdown inhibits the proliferation of EJ cells. (B) MTT test after *TRIM59* overexpression promotes the proliferation of 5637 cells. (C) Invasion assay after *TRIM59* knockdown inhibits the proliferation of EJ cells (Scale bar = 100 μ m). (D) Invasion assay after *TRIM59* overexpression promotes the proliferation of 5637 cells (Scale bar = 100 μ m). (E) Wound healing test after *TRIM59* knockdown inhibits the proliferation of EJ cells (Scale bar = 200 μ m). (F) Wound healing test after *TRIM59* overexpression promotes the proliferation of 5637 cells (Scale bar = 200 μ m). (G) *TRIM59* knockdown enhances the protein level of ACSL4 and decreases *TRIM59*, SLC7A11, and GPX4 levels in EJ cells. (H–K) Quantification of (G). (L) *TRIM59* overexpression decreases the protein level of ACSL4 and enhances *TRIM59*, SLC7A11, and GPX4 levels in 5637 cells. (M–P) Quantification of (L). (Q) *TRIM59* knockdown enhances the RNA level of *ACSL4* and decreases *TRIM59*, *SLC7A11*, and *GPX4* levels in EJ cells. (R) *TRIM59* overexpression decreases the RNA level of *ACSL4* and enhances *TRIM59*, *SLC7A11*, and *GPX4* levels in 5637 cells. ** $p < 0.01$, *** $p < 0.001$, **** $p < 0.0001$.

RSL3 treatment, indicating that *TRIM59* knockdown promotes ferroptosis in RSL3-treated EJ cells (Fig. 11D,H).

Given that JKE-1647 is more easily metabolized *in vivo* and induces ferroptosis, we chose JKE-1647 as the ferroptosis inducer for *in vivo* experiments. We developed a subcutaneous tumor model using EJ cells, dividing them into four groups: sh control, sh control with JKE-1647, sh *TRIM59*, and sh *TRIM59* with JKE-1647/atezolizumab. Consistent with *in vitro* results, ferroptosis activation significantly inhibited subcutaneous tumor growth, and the combination of JKE-1647/atezolizumab and sh *TRIM59* had a stronger inhibitory effect than JKE-1647 alone. The combination of *TRIM59* knockdown with JKE-1647 and ate-

zolizumab significantly inhibited BCa subcutaneous tumor growth (Fig. 11I,J), suggesting that *TRIM59* knockdown enhances ferroptosis activation. The absence of significant differences in plasma *ALT* and *AST* levels across the groups indicates that JKE-1647/atezolizumab does not induce hepatotoxicity (Fig. 11K,L).

4. Discussion

A multitude of expression variations influenced by cis- or trans-eQTLs can be explained by differences in genotype frequencies at specific loci. Germline genetic variants have been found to partially account for mRNA expression discrepancies across various cancer types, such

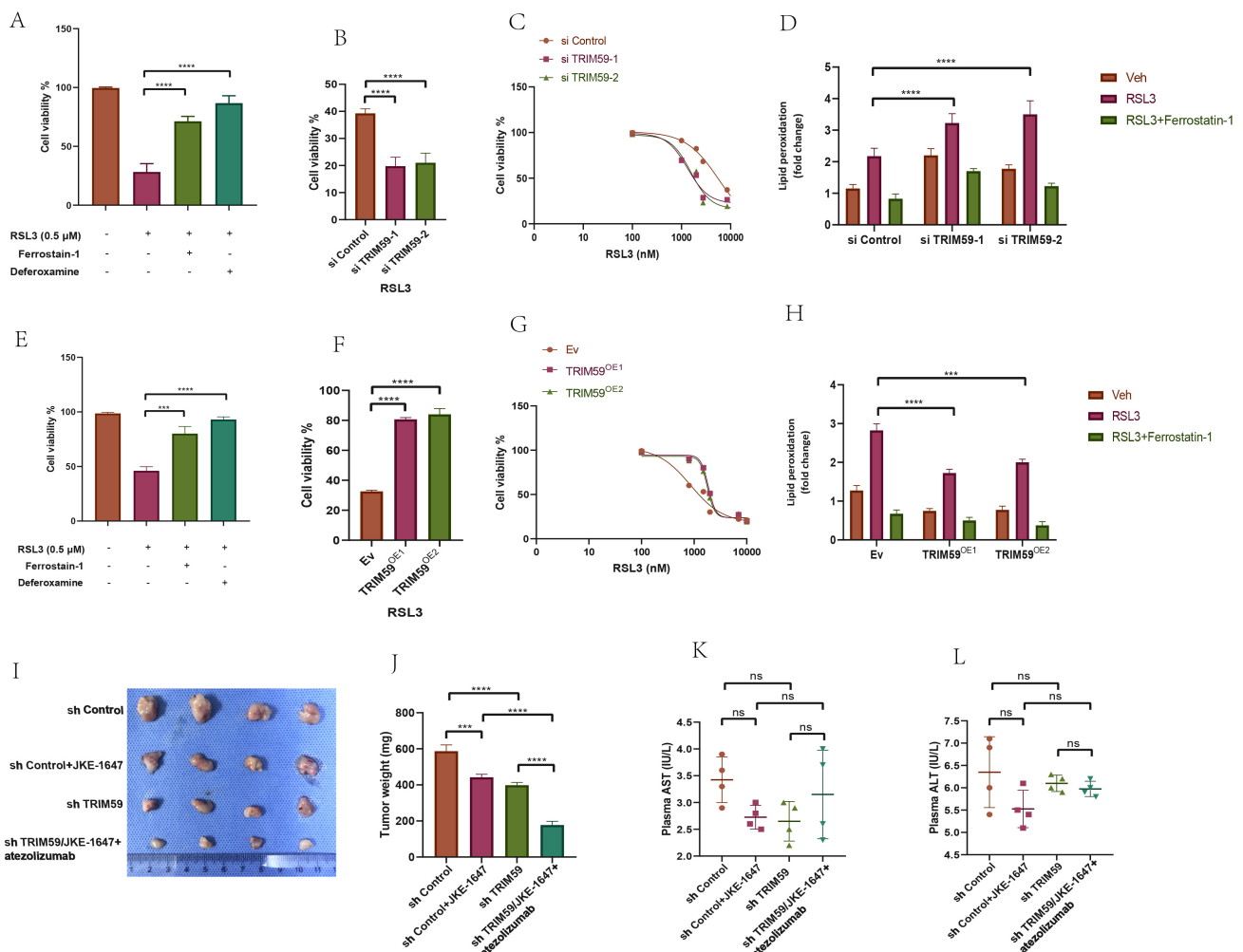


Fig. 11. Determination of the effect of *TRIM59* on the level of ferroptosis of BCa cells and effect of JKE-1647/atezolizumab on the growth of subcutaneous transplanted tumors in nude mice. ((A) EJ, (E) 5637) Cell viability analyses of different groups of two BCa cells treated with ferroptosis activators or ferroptosis inhibitors. (B,C,F,G) Detection of IC₅₀ values of RSL3 after knockdown or overexpression of *TRIM59* by cell viability analyses. (D,H) Detection of lipid peroxidation levels after application of RSL3 or Ferrostain-1 in knockdown or overexpression of *TRIM59* BCa cells. (I,J) Construction of CDX models and assessment of tumor weight in various mice groups of EJ cells. (K,L) Detection of liver function in different groups of nude mice. *** $p < 0.001$, **** $p < 0.0001$, ns > 0.05 .

as BCa, in a population-dependent manner [23]. The research highlighted 221 m6A-SNPs that exhibited eQTL associations with BCa, notably the rs3088107 (C > G) variant within the ring finger protein, transmembrane 2 (*RNFT2*) gene, which showed a strong eQTL effect by reducing *RNFT2* expression levels and m6A methylation, indicating that m6A-SNPs may function as promising biomarkers for BCa diagnosis and prognosis [24]. Furthermore, three functional SNPs—ribosomal protein S6 kinase B1 (*RPS6KB1*) rs1292038, phosphoinositide-3-kinase regulatory subunit 1 (*PIK3RI*) rs34303, and rs56352616—were found to be associated with a higher risk of developing BCa, where individuals carrying more risk alleles demonstrated greater disease susceptibility [25]. Additionally, variations in the long non-coding RNA (lncRNA) Prostate Cancer Associated Transcript 1 (*PCAT1*) gene, particularly the SNP

rs710886, have been associated with susceptibility to BCa, suggesting their potential as biomarkers for assessing BCa risk [26]. The research further demonstrated notable genetic interactions between SNPs and BCa, with patterns resembling those seen in SNP pairs linked to Alzheimer's disease. Analysis of the ENCODE dataset indicated that these SNPs likely influence common biological pathways through mechanisms involving transcription factor binding sites and chromatin interactions, thereby identifying novel potential therapeutic targets for BCa and related conditions [27]. Inherited SNPs play a crucial role in influencing cancer-related immune characteristics and treatment responses, as evidenced by a total of 103 germline gene signature quantitative trait loci (gsQTLs) identified in this study. This discovery provides a useful foundation for integrating germline genetic information into tailored im-

munotherapeutic strategies [28]. Consequently, combining genomic, epigenomic, and transcriptomic data—including eQTL analyses of both tumor and host tissues in BCa patients—deepens our understanding of BCa development and emphasizes the critical role of multi-omics integration in advancing cancer research [29]. This work presents a comprehensive approach that merges genomic, transcriptomic, and eQTL data to investigate BCa and its tumor immune microenvironment, offering a multidimensional perspective on the disease.

An analysis of distinct signaling pathways between high-risk and low-risk cohorts revealed significant variations in underlying molecular mechanisms. Molecules of cell adhesion has the important function on cancer development and progression by promoting trans-endothelial migration (TEM) of tumor cells, EMT, and epigenetic modifications, all of which aid in immune escape and metastasis [30]. Moreover, in many cancers harboring p53 mutations, such as BCa, the repair of DNA damage largely relies on the G2/M checkpoint. Disruption of this checkpoint can lead to unresolved DNA damage, forcing cells into mitotic catastrophe and ultimately triggering apoptosis. On the other hand, hyperactivation of the G2/M checkpoint enables cancer cells to endure and fosters tumor advancement [31]. The high-risk group exhibited significant involvement of pathways associated with “cell-cell adhesion mediator activity”, “cell cycle regulation”, and “mismatch repair”, indicating a greater likelihood of malignant evolution in these individuals. Gene Set Enrichment Analysis further confirmed the overrepresentation of the “EMT” and “G2M checkpoint” pathways, supporting this observation. The low-risk cohort exhibited heightened activity in various metabolic pathways, particularly those related to ‘arachidonic acid metabolism’ and ‘estrogen metabolism’. Arachidonic acid (AA) and its metabolites, generated through interactions with extracellular molecules via sPLA2, are essential components of the cellular microenvironment, significantly influencing immune responses and the development of cancer [32]. In AA metabolism, COX and LOXs enzymes are critically involved, with their expression levels varying across tumor tissues. Specifically, COX-2 contributes to tumor advancement by promoting inflammation, angiogenesis, and cell proliferation [33], while LOXs isoforms, such as 5-LOX, 12-LOX, and 15-LOX, facilitate the synthesis of LTs and HETEs, which in turn support tumor cell growth and vascularization, enhancing overall tumor biological activity [34,35]. On the other hand, estrogen receptor- α and estrogen receptor- β have been linked to the onset and progression of urothelial carcinoma, also affecting the response to chemotherapy in BCa [36]. These observations suggest that the low-risk group may possess greater metabolic flexibility and improved tumor differentiation features. Collectively, these results highlight the significant correlation between the risk classification of BCa patients and the molecular traits of their tumors, particu-

larly in terms of metabolic activity, shedding light on the distinct molecular mechanisms underlying tumor progression in high- versus low-risk groups.

BCa encompasses several molecular subtypes, including luminal-papillary, luminal-infiltrated, basal-squamous, and neuronal, each displaying distinct molecular and pathological characteristics [37]. The luminal-papillary subtype makes up approximately 35% of all cases and is defined by papillary histology. It is frequently associated with *FGFR3* mutations, amplifications, or gene fusions, as well as activation of the Sonic Hedgehog signaling pathway. This subtype is generally linked to a lower likelihood of disease progression and a reduced sensitivity to neoadjuvant chemotherapy (NAC). Given the prevalence of *FGFR3* alterations, targeted treatment options such as *FGFR3*-specific or pan-FGFR inhibitors—Erdafitinib, for instance—may offer therapeutic benefits. The luminal-infiltrated subtype accounts for about 19% of cases and is distinguished by low tumor purity along with substantial infiltration of immune and stromal cells. It also demonstrates elevated expression levels of *PD-L1* and cytotoxic T-lymphocyte-associated protein 4 (*CTLA4*), suggesting that immunotherapeutic approaches, particularly immune checkpoint inhibitors, could be effective, even though this subtype typically responds poorly to standard platinum-based chemotherapy. The basal-squamous subtype, present in roughly 35% of cases, is more frequently observed in women and is marked by squamous differentiation. It also shows high expression of *PD-L1* and *CTLA4*, along with significant immune and stromal cell infiltration, indicating potential responsiveness to both platinum-based chemotherapy and immunotherapy [38]. Through an analysis of BCa molecular subtypes, our findings reveal that the risk model successfully differentiates among these subtypes. The basal-like subtype is primarily represented in the high-risk category, whereas the luminal-like subtype is more common in the low-risk group. A comparative assessment of key gene mutations across the two risk groups highlighted significant variations in the mutation patterns and allele frequencies of *TP53*, *TTN*, and *PIK3CA*. Combining the risk model with molecular subtype classification enhances the accuracy of prognostic predictions, offering valuable insights for the clinical management of BCa.

The immune microenvironment of BCa plays a crucial role in both the onset and progression of the disease. Within this microenvironment, macrophages exhibit a range of functional states, broadly classified into two types: M1 macrophages, which have tumor-suppressive properties, and M2 macrophages, which support tumor growth [39]. M2 macrophages, often recognized by the presence of markers such as CD163 and IL-10, are frequently found in high numbers within the tumor area and are associated with worse clinical outcomes in BCa patients [40]. Studies suggest that combining PD-L1 blockade with TGF- β inhibition can enhance anti-tumor immunity and improve

survival outcomes [41,42]. CD8+ T cells are also central players in the immune response against cancer, acting as primary mediators of tumor cell destruction across various malignancies. Among them, the CD8+, CD103+ subset demonstrates a strong association with tumor-specific reactivity, exhibiting potent cytotoxic activity via Major Histocompatibility Complex (*MHC*) class I-dependent mechanisms [43,44]. Our findings revealed that the high-risk cohort demonstrated a heightened capacity for immune escape, marked by increased infiltration of macrophages and fibroblasts, while the low-risk group exhibited enhanced CD8+ T cell activity. This suggests that individuals in the high-risk category may employ immunosuppressive mechanisms to evade immune surveillance, thereby promoting tumor progression. The increased expression of T cell receptor-related checkpoints and inhibitory co-factors, such as *CD276* and *PVR*, further underscores the immune evasive profile of the high-risk group. Evaluating immune cell infiltration patterns and immune escape potential provides meaningful insights into the BCa immune microenvironment and highlights potential biomarkers for predicting immunotherapy effectiveness. Investigating the relationship between risk models and responsiveness to chemotherapeutic agents offers essential guidance for tailored BCa treatment approaches. Our results suggest that patients at high risk are less responsive to several commonly used chemotherapy drugs, including crizotinib and temsirolimus, which may be attributed to the aggressive tumor behavior and advanced immune evasion tactics in this group. Conversely, the low-risk group displayed greater sensitivity to agents such as cyclophosphamide, cytarabine, and paclitaxel, offering clinicians useful information for selecting optimal therapeutic strategies. Assessing the association between riskScores and drug sensitivity improves the predictive accuracy of chemotherapy responses, thus facilitating more precise and individualized treatment planning.

Ferroptosis represents a recently characterized form of regulated cell death, primarily distinguished by its reliance on iron and the buildup of lipid reactive oxygen species [45]. In cancer contexts, ferroptosis is modulated by multiple signaling pathways, including but not limited to Nuclear Factor Erythroid 2-Related Factor 2 (Nrf2), p53, heme oxygenase-1, Autophagy-related gene 6 (*BECN1*), and Fanconi anemia, complementation group D2 (*FANCD2*) [46]. Our findings reveal that *TRIM59* promotes the expression of SLC7A11 and GPX4, two key proteins that act to suppress ferroptosis. SLC7A11 functions as a cystine transporter, facilitating the synthesis of glutathione and enhancing cellular antioxidant defenses [47,48]. It is widely acknowledged as a negative regulator of ferroptosis and is frequently overexpressed in various malignancies [49]. Elevated levels of SLC7A11 have been associated with tumor development through both ferroptosis-dependent and independent mechanisms. Our experimental data demonstrated that silencing *TRIM59* reduced the expression of SLC7A11 and GPX4 in

BCa cells, both in cultured cell models and in animal models. Moreover, *TRIM59* knockdown increased the sensitivity of BCa cells to DOX treatment by promoting ferroptotic cell death.

By combining genomic, eQTL, and transcriptomic data, we have developed a comprehensive risk model that deepens our understanding of the molecular mechanisms underlying BCa and its tumor immune microenvironment, thus facilitating more precise treatment approaches. This research provides novel perspectives on the molecular characteristics of BCa and establishes a foundation for tailored therapeutic interventions. Through an in-depth analysis of the connections between the BCa risk model, immune microenvironment, response to chemotherapy, and clinical outcomes, we present meaningful tools to support future personalized management and treatment of BCa patients. However, certain limitations of this study must be acknowledged. The findings may have limited applicability across broader populations due to the specific demographic characteristics of the samples used, highlighting the need for further large-scale, multi-center investigations. Additionally, while associations between genetic variations and different risk categories have been identified, more research is necessary to uncover the specific mechanisms at play within BCa subtypes.

5. Conclusions

This research has established a screening framework aimed at uncovering cellular diversity within the ferroptosis and immune microenvironment influenced by BCa, while also identifying novel biomarker candidates. The findings emphasize the critical role of *TRIM59* in the progression of BCa. Increased expression of *TRIM59* correlates with tumor development and resistance to chemotherapy in BCa cases. Suppressing *TRIM59* could potentially promote ferroptosis in BCa cells, thereby improving their responsiveness to DOX. Combining ferroptosis-triggering agents with immunotherapeutic strategies targeting *TRIM59* may offer a viable treatment option for BCa. Furthermore, progress in precision medicine—leveraging combined genomic, transcriptomic, and clinical data—will support the development of tailored therapeutic approaches for individuals with BCa.

Availability of Data and Materials

The datasets used and analyzed during the current study are available from the corresponding author on reasonable request.

Author Contributions

Conceptualization, JL, XW, HL, PW, YQ, XZ, and PZ; material preparation, JL, PW and YQ; writing original draft preparation, JL, XZ and PZ; writing, editing and review, JL and HL. All authors contributed to editorial changes in the manuscript. All authors read and approved

the final manuscript. All authors have participated sufficiently in the work and agreed to be accountable for all aspects of the work.

Ethics Approval and Consent to Participate

This study was approved by the Animal Ethics Committee of Tianjin Medical University. Our *in vivo* studies strictly follow the “ARRIVE and PREPARE” guidelines. All experiments were conducted in accordance with relevant guidelines and regulations (IRB2019-KY-086). The TCGA and GEO databases are open access and freely available to all researchers, in compliance with ethical guidelines.

Acknowledgment

We acknowledge the TCGA and GEO databases and their contributors.

Funding

This work was supported by the Research Project of Tianjin Medical University Cancer Institute & Hospital (NO. Y1715, Y1904, Y1905), Tianjin Key Medical Discipline (Specialty) Construction Project (TJYXZDXK-009A).

Conflict of Interest

The authors declare no conflict of interest.

Supplementary Material

Supplementary material associated with this article can be found, in the online version, at <https://doi.org/10.31083/FBL44395>.

References

- [1] Sung H, Ferlay J, Siegel RL, Laversanne M, Soerjomataram I, Jemal A, *et al.* Global Cancer Statistics 2020: GLOBOCAN Estimates of Incidence and Mortality Worldwide for 36 Cancers in 185 Countries. *CA: a Cancer Journal for Clinicians*. 2021; 71: 209–249. <https://doi.org/10.3322/caac.21660>.
- [2] Liu S, Chen X, Lin T. Emerging strategies for the improvement of chemotherapy in bladder cancer: Current knowledge and future perspectives. *Journal of Advanced Research*. 2022; 39: 187–202. <https://doi.org/10.1016/j.jare.2021.11.010>.
- [3] Flaig TW, Spiess PE, Agarwal N, Bangs R, Boorjian SA, Buyounouski MK, *et al.* NCCN Guidelines Insights: Bladder Cancer, Version 5.2018. *Journal of the National Comprehensive Cancer Network*. 2018; 16: 1041–1053. <https://doi.org/10.6004/jnccn.2018.0072>.
- [4] Lenis AT, Lec PM, Chamie K, Mshs MD. Bladder Cancer: A Review. *JAMA*. 2020; 324: 1980–1991. <https://doi.org/10.1001/jama.2020.17598>.
- [5] Tran L, Xiao JF, Agarwal N, Duex JE, Theodorescu D. Advances in bladder cancer biology and therapy. *Nature Reviews. Cancer*. 2021; 21: 104–121. <https://doi.org/10.1038/s41568-020-00313-1>.
- [6] Cathomas R, Lorch A, Bruins HM, Comp  rat EM, Cowan NC, Efstathiou JA, *et al.* The 2021 Updated European Association of Urology Guidelines on Metastatic Urothelial Carcinoma. *European Urology*. 2022; 81: 95–103. <https://doi.org/10.1016/j.eururo.2021.09.026>.
- [7] Leyderman M, Chandrasekar T, Grivas P, Li R, Bhat S, Basnet A, *et al.* Metastasis development in non-muscle-invasive bladder cancer. *Nature Reviews. Urology*. 2025; 22: 375–386. <https://doi.org/10.1038/s41585-024-00963-y>.
- [8] Lopez-Beltran A, Cookson MS, Guercio BJ, Cheng L. Advances in diagnosis and treatment of bladder cancer. *BMJ (Clinical Research Ed.)*. 2024; 384: e076743. <https://doi.org/10.1136/bmj-2023-076743>.
- [9] Katoh M, Lorient Y, Brandi G, Tavolari S, Wainberg ZA, Katoh M. FGFR-targeted therapeutics: clinical activity, mechanisms of resistance and new directions. *Nature Reviews. Clinical Oncology*. 2024; 21: 312–329. <https://doi.org/10.1038/s41571-024-00869-z>.
- [10] Picard LC, Rich FJ, Kenwright DN, Stevens AJ. Epigenetic changes associated with Bacillus Calmette-Gu  rin (BCG) treatment in bladder cancer. *Biochimica et Biophysica Acta. Reviews on Cancer*. 2024; 1879: 189123. <https://doi.org/10.1016/j.bbcan.2024.189123>.
- [11] Liu Q, Guan Y, Li S. Programmed death receptor (PD)-1/PD-ligand (L)1 in urological cancers: the “all-around warrior” in immunotherapy. *Molecular Cancer*. 2024; 23: 183. <https://doi.org/10.1186/s12943-024-02095-8>.
- [12] Nadal R, Valderrama BP, Bellmunt J. Progress in systemic therapy for advanced-stage urothelial carcinoma. *Nature Reviews. Clinical Oncology*. 2024; 21: 8–27. <https://doi.org/10.1038/s41571-023-00826-2>.
- [13] Choi W, Porten S, Kim S, Willis D, Plimack ER, Hoffman-Censits J, *et al.* Identification of distinct basal and luminal subtypes of muscle-invasive bladder cancer with different sensitivities to frontline chemotherapy. *Cancer Cell*. 2014; 25: 152–165. <https://doi.org/10.1016/j.ccr.2014.01.009>.
- [14] Damrauer JS, Hoadley KA, Chism DD, Fan C, Tiganelli CJ, Wobker SE, *et al.* Intrinsic subtypes of high-grade bladder cancer reflect the hallmarks of breast cancer biology. *Proceedings of the National Academy of Sciences of the United States of America*. 2014; 111: 3110–3115. <https://doi.org/10.1073/pnas.1318376111>.
- [15] Mo Q, Nikolos F, Chen F, Tramel Z, Lee YC, Hayashi K, *et al.* Prognostic Power of a Tumor Differentiation Gene Signature for Bladder Urothelial Carcinomas. *Journal of the National Cancer Institute*. 2018; 110: 448–459. <https://doi.org/10.1093/jnci/djx243>.
- [16] Rebouissou S, Bernard-Pierrot I, de Reyni  s A, Lepage ML, Krucker C, Chapeaublanc E, *et al.* EGFR as a potential therapeutic target for a subset of muscle-invasive bladder cancers presenting a basal-like phenotype. *Science Translational Medicine*. 2014; 6: 244ra91. <https://doi.org/10.1126/scitranslmed.3008970>.
- [17] Robertson AG, Kim J, Al-Ahmadie H, Bellmunt J, Guo G, Cherniack AD, *et al.* Comprehensive Molecular Characterization of Muscle-Invasive Bladder Cancer. *Cell*. 2018; 174: 1033. <https://doi.org/10.1016/j.cell.2018.07.036>.
- [18] Sj  dahl G, Lauss M, L  vgren K, Chebil G, Gudjonsson S, Veerla S, *et al.* A molecular taxonomy for urothelial carcinoma. *Clinical Cancer Research*. 2012; 18: 3377–3386. <https://doi.org/10.1158/1078-0432.CCR-12-0077-T>.
- [19] Kamoun A, de Reyni  s A, Allory Y, Sj  dahl G, Robertson AG, Seiler R, *et al.* A Consensus Molecular Classification of Muscle-Invasive Bladder Cancer. *European Urology*. 2020; 77: 420–433. <https://doi.org/10.1016/j.eururo.2019.09.006>.
- [20] Jia Q, Wu W, Wang Y, Alexander PB, Sun C, Gong Z, *et al.* Local mutational diversity drives intratumoral immune heterogeneity in non-small cell lung cancer. *Nature Communications*. 2018; 9: 5361. <https://doi.org/10.1038/s41467-018-07767-w>.

- [21] Jiang P, Gu S, Pan D, Fu J, Sahu A, Hu X, *et al.* Signatures of T cell dysfunction and exclusion predict cancer immunotherapy response. *Nature Medicine*. 2018; 24: 1550–1558. <https://doi.org/10.1038/s41591-018-0136-1>.
- [22] Geeleher P, Cox N, Huang RS. pRRophetic: an R package for prediction of clinical chemotherapeutic response from tumor gene expression levels. *PLoS ONE*. 2014; 9: e107468. <https://doi.org/10.1371/journal.pone.0107468>.
- [23] Carrot-Zhang J, Chambwe N, Damrauer JS, Knijnenburg TA, Robertson AG, Yau C, *et al.* Comprehensive Analysis of Genetic Ancestry and Its Molecular Correlates in Cancer. *Cancer Cell*. 2020; 37: 639–654. <https://doi.org/10.1016/j.ccell.2020.04.012>.
- [24] Lv J, Song Q, Bai K, Han J, Yu H, Li K, *et al.* N6-methyladenosine-related single-nucleotide polymorphism analyses identify oncogene RNFT2 in bladder cancer. *Cancer Cell International*. 2022; 22: 301. <https://doi.org/10.1186/s12935-022-02701-z>.
- [25] Ma L, Zhang D, Huang Z, Zheng R, Du M, Lv Q, *et al.* Functional variants of RPS6KB1 and PIK3R1 in the autophagy pathway genes and risk of bladder cancer. *Archives of Toxicology*. 2022; 96: 367–375. <https://doi.org/10.1007/s00204-021-03173-2>.
- [26] Lin Y, Ge Y, Wang Y, Ma G, Wang X, Liu H, *et al.* The association of rs710886 in lncRNA PCAT1 with bladder cancer risk in a Chinese population. *Gene*. 2017; 627: 226–232. <https://doi.org/10.1016/j.gene.2017.06.021>.
- [27] Li H, Achour I, Bastarache L, Berghout J, Gardeux V, Li J, *et al.* Integrative genomics analyses unveil downstream biological effectors of disease-specific polymorphisms buried in intergenic regions. *NPJ Genomic Medicine*. 2016; 1: 16006. <https://doi.org/10.1038/npjgenmed.2016.6>.
- [28] Lim YW, Chen-Harris H, Mayba O, Lianoglou S, Wuster A, Bhargale T, *et al.* Germline genetic polymorphisms influence tumor gene expression and immune cell infiltration. *Proceedings of the National Academy of Sciences of the United States of America*. 2018; 115: E11701–E11710. <https://doi.org/10.1073/pnas.1804506115>.
- [29] Pineda S, Van Steen K, Malats N. Integrative eQTL analysis of tumor and host omics data in individuals with bladder cancer. *Genetic Epidemiology*. 2017; 41: 567–573. <https://doi.org/10.1002/gepi.22053>.
- [30] Qian WJ, Yan JS, Gang XY, Xu L, Shi S, Li X, *et al.* Inter-cellular adhesion molecule-1 (ICAM-1): From molecular functions to clinical applications in cancer investigation. *Biochimica et Biophysica Acta. Reviews on Cancer*. 2024; 1879: 189187. <https://doi.org/10.1016/j.bbcan.2024.189187>.
- [31] Yan J, Zhuang L, Wang Y, Jiang Y, Tu Z, Dong C, *et al.* Inhibitors of cell cycle checkpoint target Wee1 kinase - a patent review (2003-2022). *Expert Opinion on Therapeutic Patents*. 2022; 32: 1217–1244. <https://doi.org/10.1080/13543776.2022.2166827>.
- [32] Hidalgo I, Sorolla MA, Sorolla A, Salud A, Parisi E. Secreted Phospholipases A2: Drivers of Inflammation and Cancer. *International Journal of Molecular Sciences*. 2024; 25: 12408. <https://doi.org/10.3390/ijms252212408>.
- [33] Moon H, White AC, Borowsky AD. New insights into the functions of Cox-2 in skin and esophageal malignancies. *Experimental & Molecular Medicine*. 2020; 52: 538–547. <https://doi.org/10.1038/s12276-020-0412-2>.
- [34] Wan M, Tang X, Stsianava A, Haeggström JZ. Biosynthesis of leukotriene B₄. *Seminars in Immunology*. 2017; 33: 3–15. <https://doi.org/10.1016/j.smim.2017.07.012>.
- [35] Lu W, Aihaiti A, Abudukeranu P, Liu Y, Gao H. Arachidonic acid metabolism as a novel pathogenic factor in gastrointestinal cancers. *Molecular and Cellular Biochemistry*. 2025; 480: 1225–1239. <https://doi.org/10.1007/s11010-024-05057-2>.
- [36] Goto T, Miyamoto H. The Role of Estrogen Receptors in Urothelial Cancer. *Frontiers in Endocrinology*. 2021; 12: 643870. <https://doi.org/10.3389/fendo.2021.643870>.
- [37] Pereira F, Domingues MR, Vitorino R, Guerra IMS, Santos LL, Ferreira JA, *et al.* Unmasking the Metabolite Signature of Bladder Cancer: A Systematic Review. *International Journal of Molecular Sciences*. 2024; 25: 3347. <https://doi.org/10.3390/ijms25063347>.
- [38] Iacovino ML, Miceli CC, De Felice M, Barone B, Pompella L, Chiancone F, *et al.* Novel Therapeutic Opportunities in Neoadjuvant Setting in Urothelial Cancers: A New Horizon Opened by Molecular Classification and Immune Checkpoint Inhibitors. *International Journal of Molecular Sciences*. 2022; 23: 1133. <https://doi.org/10.3390/ijms23031133>.
- [39] DeNardo DG, Ruffell B. Macrophages as regulators of tumour immunity and immunotherapy. *Nature Reviews. Immunology*. 2019; 19: 369–382. <https://doi.org/10.1038/s41577-019-0127-6>.
- [40] Koll FJ, Banek S, Kluth L, Köllermann J, Bankov K, Chun FKH, *et al.* Tumor-associated macrophages and Tregs influence and represent immune cell infiltration of muscle-invasive bladder cancer and predict prognosis. *Journal of Translational Medicine*. 2023; 21: 124. <https://doi.org/10.1186/s12967-023-03949-3>.
- [41] Mariathasan S, Turley SJ, Nickles D, Castiglioni A, Yuen K, Wang Y, *et al.* TGF β attenuates tumour response to PD-L1 blockade by contributing to exclusion of T cells. *Nature*. 2018; 554: 544–548. <https://doi.org/10.1038/nature25501>.
- [42] van Dorp J, van der Heijden MS. The bladder cancer immune micro-environment in the context of response to immune checkpoint inhibition. *Frontiers in Immunology*. 2023; 14: 1235884. <https://doi.org/10.3389/fimmu.2023.1235884>.
- [43] Wang J, Lu Q, Chen X, Aifantis I. Targeting MHC-I inhibitory pathways for cancer immunotherapy. *Trends in immunology*. 2024; 45: 177–187. <https://doi.org/10.1016/j.it.2024.01.009>.
- [44] Rizvi H, Sanchez-Vega F, La K, Chatila W, Jonsson P, Halpenny D, *et al.* Molecular Determinants of Response to Anti-Programmed Cell Death (PD)-1 and Anti-Programmed Death-Ligand 1 (PD-L1) Blockade in Patients With Non-Small-Cell Lung Cancer Profiled With Targeted Next-Generation Sequencing. *Journal of Clinical Oncology*. 2018; 36: 633–641. <https://doi.org/10.1200/JCO.2017.75.3384>.
- [45] Jiang X, Stockwell BR, Conrad M. Ferroptosis: mechanisms, biology and role in disease. *Nature Reviews. Molecular Cell Biology*. 2021; 22: 266–282. <https://doi.org/10.1038/s41580-020-00324-8>.
- [46] Wang Y, Wu N, Li J, Liang J, Zhou D, Cao Q, *et al.* The interplay between autophagy and ferroptosis presents a novel conceptual therapeutic framework for neuroendocrine prostate cancer. *Pharmacological Research*. 2024; 203: 107162. <https://doi.org/10.1016/j.phrs.2024.107162>.
- [47] Shen L, Zhang J, Zheng Z, Yang F, Liu S, Wu Y, *et al.* PHGDH Inhibits Ferroptosis and Promotes Malignant Progression by Up-regulating SLC7A11 in Bladder Cancer. *International Journal of Biological Sciences*. 2022; 18: 5459–5474. <https://doi.org/10.7150/ijbs.74546>.
- [48] Lv T, Fan X, He C, Zhu S, Xiong X, Yan W, *et al.* SLC7A11-ROS/ α KG-AMPK axis regulates liver inflammation through mitophagy and impairs liver fibrosis and NASH progression. *Redox Biology*. 2024; 72: 103159. <https://doi.org/10.1016/j.redox.2024.103159>.
- [49] Jiang Y, Sun M. SLC7A11: the Achilles heel of tumor? *Frontiers in Immunology*. 2024; 15: 1438807. <https://doi.org/10.3389/fimmu.2024.1438807>.